Recommended Practices for Design and Use of Retarding Potential Analyzers in Electric Propulsion

IEPC-2025-363

Kristina M. Lemmer,[*] and Austen J. Thomas.[†]
Western Michigan University, Kalamazoo, MI, 49009, USA

Wensheng Huang[‡]
NASA Glenn Research Center, Cleveland, OH, 44135, USA

and

Dan M. Goebel[§], and Robert B. Lobbia[**]
Jet Propulsion Laboratory, California Institute of Technology, Pasadena, CA, 91109, USA

Abstract: Retarding potential analyzers (RPAs) are relatively simple and powerful diagnostic tools that are capable of providing ion energy distribution functions within the plume of an electric propulsion thruster. The purpose of this paper is to provide a guide to standardize RPA design, construction, operation, error analysis, and data interpretation for operation within the plasma environment produced by an electric propulsion thruster. Operational environment, correction factors, and error analysis are presented along with time-averaged and time resolved probe operation and data analysis methods. These best practices have been compiled from extensive experience using RPAs for electric propulsion thruster testing and previous publications on the design, use, and analysis of data from RPA probes. Focus in this guide is placed on the use of RPAs in the most common electric propulsion devices, namely Hall effect thrusters, where the plasma is flowing and ions have a rich variety of energy and oscillatory behaviors. The strategies presented in this guide are expected to increase the quality and repeatability of testing data obtained from electric propulsion systems, thereby allowing for improved comparisons between different thrusters and operating environments and improving the fidelity of models for on-orbit predictions.

Nomenclature

$A_x^*(k)$	=	arbitrary Fourier coefficient
a_{grid}	=	wire center separation, m
$A_{y_{syn}}(k)$	=	synthetic Fourier coefficient
A_b	=	beamlet cross sectional area, m^2
$A_x(k), A_y(k)$	=	Fourier coefficient

[*] Professor, Mechanical and Aerospace Engineering.
[†] Ph.D. Candidate, Mechanical and Aerospace Engineering.
[‡] Research Engineer, Electric Propulsion Systems Branch
[§] Senior Research Scientist, Electric Propulsion Group.
[**] Senior Electric Propulsion Engineer, Electric Propulsion Group.

C	=	capacitance, F
C*	=	geometric term related to electron repelling grid
Ω_{RPA}	=	solid angle field of view
d	=	distance between thruster exit and RPA entrance, m
d_a	=	electron repelling grid diameter, m
$d\boldsymbol{A}$	=	differential surface area element, m
ΔV	=	potential difference between aperture axis and aperture wall, V
$\Delta V_{r,sag}$	=	deviation or "sag" in retarding grid potential, V
$\Delta V_{r,fov}$	=	deviation or "sag" in effective retarding potential from field-of-view, V
e	=	electron charge, 1.602 x 10^-19 C
$\mathbf{E}$	=	electric field, V/m
E	=	SMI embedding dimension
$\mathcal{E}$	=	ion energy, J
ε_o	=	permittivity of free space. 8.85 x 10^-12 F/m
η_V	=	voltage utilization efficiency
$\dot{h}_x$	=	erosion rate, m/s
$\mathcal{H}$	=	transfer function
h_{RPA}	=	distance between inlet and collector of RPA, m
I_{disp}	=	displacement current, A
I_c	=	current to collector, A
I_e	=	electron current inside analyzer, A
I_i	=	ion current inside analyzer, A
I_{ref}	=	reference current for TF and SMI reconstruction
J_{total}	=	current density, A/m^2
k	=	Boltzmann's constant, 1.38 x 10^-23 J/K, or frequency bin, Hz
λ_D	=	Debye length, m
m	=	electron mass, kg
M	=	ion mass, kg
$\widehat{M}_{\tilde{y}(t)}$	=	reconstructed synthetic shadow manifold
M_x, $M_{\tilde{x}}$, M_y	=	shadow manifold
$\mathcal{N}$	=	nearest neighbor
n_e	=	electron number density, m^{-3}
n_i	=	ion plasma density, m^{-3}
$r_{collector}$	=	RPA collector radius, m
r_{grid}	=	wire radius, m
r_{inlet}	=	RPA inlet radius, m
t	=	time
t_a	=	grid transparency
t_{dwell}	=	ion dwell time in the RPA, s
t_{tof}	=	time of flight, s
τ	=	time lag of time series
T_e	=	electron temperature, eV
θ_{fov}	=	field-of-view half angle, degree
V	=	potential difference between grids, V
V_D	=	Discharge voltage, V
V_{ion}	=	ion beam potential, V
V_a	=	applied electron repelling grid potential, V
V_i	=	plasma potential at analyzer entrance, V
v_i	=	ion velocity, m/s

V_m	=	minimum potential in analyzer, V
V_m*	=	minimum potential in analyzer neglecting space charge effects, V
V_p	=	plasma potential, V
V_r	=	discriminator grid bias (retarding potential), V
w_i	=	normalized weights
x	=	grid separation distance between electron repelling and ion discriminator, m
$X(t)$, $Y(t)$	=	time series data
$x(t)$, $y(t)$	=	training time series data
x_{grids}	=	grid separation distance general, m
$\tilde{x}(t)$, $\tilde{y}(t)$	=	testing time series data
y_{syn}	=	synthetic time series reconstruction
$\tilde{y}_r(t)$	=	reconstructed output signal
Z	=	charge state

I. Introduction

RETARDING potential analyzer (RPA) probes are experimental devices commonly used to simply and effectively measure the energy of ions in a plasma. This diagnostic tool uses a series of biased grids to filter ions on the basis of kinetic energy as the particles travel through the device before reaching a collection surface where current is measured. RPAs are often used to measure the ion energy distribution function (IEDF) in electric propulsion (EP) thrusters during ground testing in vacuum chambers, and there is a strong desire to use RPAs for on-orbit measurements to understand off-axis ion energy in space. These data are used for several purposes, including 1) characterization of plasma processes in the plume of an EP thruster to analyze efficiency loss mechanisms and potential plasma-spacecraft interactions, 2) understanding EP thruster performance differences between ground testing and in-space operation, 3) validation data for EP thruster plume models and predictive engineering models, and 4) understanding plasma oscillations in different EP thruster operating conditions.

Theoretical and experimental work on retarding field energy analyzers is found in publications dating back to the 1960's[1–7]. Most of the early work centered around determining the ion energy distribution functions in glow discharges and RF plasmas. Within the EP testing community, RPAs have mostly been used to map the IEDF throughout the thruster plume where the probe is mounted on motion stages capable of mapping the plume in up to 3 dimensions. In general, the downstream center region of the EP thruster plume consists of a single ion energy population existing at the operational energy of the thruster. However, additional lower ion energy populations emerge off-axis in the far-field that may be caused by phenomena such as charge exchange collisions. Even further off-axis is the side plume region where higher energy ions can cause significant spacecraft interactions [8]. These regions are shown in Figure 1. Furthermore, the ion energy may vary with time, requiring the use of a time-resolved diagnostic method to measure the ion energy oscillations.

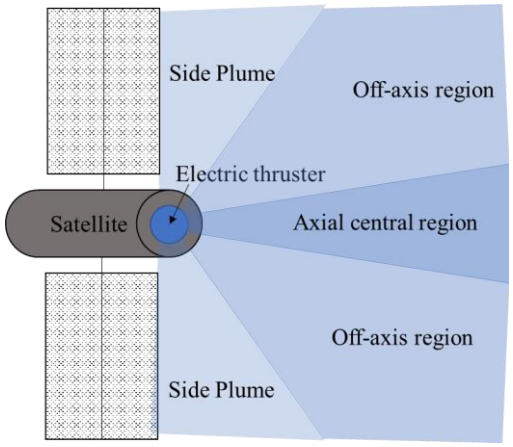

Figure 1. Regions of the plasma plume from an EP thruster such as an HET.

RPA designs utilize several different configurations and countless options for spacing and applied potential to different parts of the probe. As an example, a 4-grid RPA probe is shown in Figure 2, with the grid numbers labeled as they are described in Section III.B and example voltage magnitudes indicated. Other configurations with different numbers of grids and applied potentials may be used depending on the application. The RPA can also be used as a

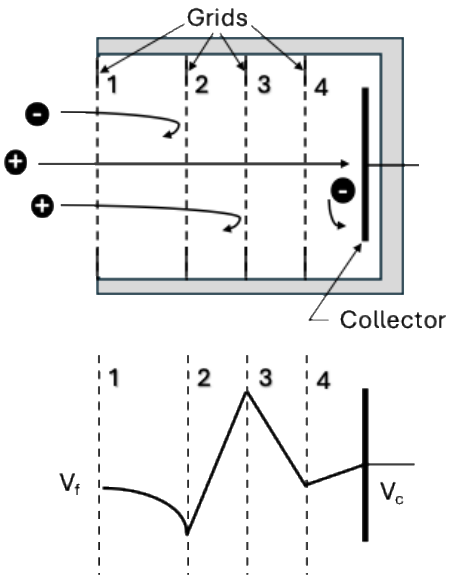

Figure 2. Schematic drawing of an RPA (top) with bias voltage magnitudes applied to grids (bottom).

diagnostic to determine ion current density, plasma potential, and secondary electron emission yields from surfaces within the testing facility [7,9].

This paper provides recommendations for time-averaged and time-resolved RPA measurements, data analysis techniques, and data interpretation, including suggested test methodologies and diagnostic design. Section II discusses the applicability of RPA probes for EP thruster testing, including how the measured data can aid in EP thruster design and operation. Section III provides an in-depth discussion of design considerations and probe configurations for RPA use in EP. Sections IV and V present testing methodology and data analysis for both time-averaged and time-resolved measurement techniques with example data sets presented. Alternative uses for RPA probes, other than measuring ion energy distribution functions, are presented in Section VI, and a conclusion is provided in Section VII. The Appendix contains a tabulated summary of recommendations and guidelines.

II. Applicability of Retarding Potential Analyzers

RPAs are a well-known plasma diagnostic used for measuring ion energy in low temperature plasmas typically found in EP systems. The RPA is used to generate a plot of collected ion current versus the ion discriminator grid voltage (retarding potential) and the derivative of this curve provides an IEDF.[††] Configurations that use multiple biased grids or apertures to provide a variable retarding electric field can provide ion energy distribution function measurements for ions in the energy range from a few electron-volts up to kilovolts of energy. RPAs can be configured with large collection areas to monitor very low-density plasma regions in and around the thruster where the ion currents are very small. Conversely, miniature RPAs can be mounted in constricted regions to allow for local measurements near cathodes and acceleration grids, or can be scanned quickly through high density plasma regions to collect ion energy data while avoiding overheating.

RPAs have may applications in EP. Those configured with larger collection areas are routinely used to measure the ion energies in the far-field plume region of thrusters to develop stay-out zones where no sensitive equipment should be placed on a spacecraft. These data can also be used to develop limits or controls for thruster spacecraft interactions. Inside the plasma generator regions of many EP thrusters, sputtering by energetic ions ultimately determines the thruster lifetime. In these regions, RPA measurements of the ion energy are used to determine the source of the energetic ions and guide the selection of materials or electrode geometries in the plasma generator to minimize the sputtering rate to provide adequate plasma generator life. Erosion measurements, $\dot{h_x}$, can be obtained from RPA IEDFs using the appropriate ion-material sputter yield curves, $Y_x(\mathcal{E})$, Ref. [10], as

$$\dot{h_x} = \frac{FW_x m_p}{e\rho_x} \int_0^{\mathcal{E}_{max}} Y_x(\mathcal{E}) IEDF(\mathcal{E}) d\mathcal{E} \tag{1}$$

where *IEDF($\mathcal{E}$)* is the function described by Eq. (24).

RPA measurements are used in both DC-discharge and RF-discharge plasma generators to measure the conditions under which ions are generated with energies above the boundary material sputtering thresholds (typically >20 eV).

[††] We note here that the RPA actually provides a measure of the ion energy per charge distribution function. This is discussed in Section V.C. For convention, we will simply call this the IEDF.

The RPA data are then used to determine whether the ions are accelerated by the DC or averaged plasma potentials in the plasma or by RF fields associated with plasma instabilities. This information can be used to select the discharge voltage, local neutral density, or RF coupling method used in the thruster in order to limit that accelerating potential. Time-resolved RPA measurements can be used to determine whether the ions have been accelerated by plasma instabilities by monitoring the time dependent collected current in the RPA in the presence of different retarding fields. The RPA data can be used to select operational parameters or optimize the geometry to damp the instabilities and limit the generation of those energetic ions. Finally, miniaturized RPAs can be placed directly in front of electrodes, such as cathode keepers and grids, to measure the impinging ion energies that cause excessive erosion. They can also be scanned into higher density regions around cathode plumes to provide ion energy profiles.

RPAs have an advantage that they are simple to construct with straightforward implementation and data analysis. However, RPAs are not capable of discriminating between the charge states of the ions. Furthermore, since an RPA is a physical probe, it will inherently affect the plasma in which it is inserted. There are other diagnostic tools capable of measuring the ion energy distribution that resolve some of these issues, but they have their own disadvantages as well. Laser induced fluorescence (LIF) is a highly capable, non-invasive diagnostic that can directly measure the ion velocity distribution function. LIF can be focused on regions that are difficult to probe, such as inside an HET discharge channel. However, LIF requires expensive laser and detection equipment and extensive, time-consuming setup. The laser must be tuned to the specific wavelength of the species being studied, whereas other probes discussed are independent of species or easily adjusted for species mass. Furthermore, LIF has a minimum detectable particle density based on the sensitivity of the detection equipment [11]. An ExB probe or Wein filter can measure the charge state of the ions in an EP thruster plume; however, the wide distribution of ion energies often results in overlapping peaks. As such, analysis requires assumptions about the shape of the distribution function that are difficult to verify [12]. Another method for measuring ion energy is the electrostatic analyzer (ESA) which uses a shaped electric field to separate ions based on their energy-to-charge ratio. An ESA has many of the same benefits and drawbacks as an RPA; however, an ESA is more difficult to build and tends to have a bigger geometric footprint within the plasma plume [13].

III.Design Considerations

The use of a retarding electric field to measure the IEDF is a relatively simple technique, but the RPA design can vary significantly depending on the application. RPAs are usually designed based on calculations of the potential distribution between the grids and in the grid apertures [9], taking into account the space charge effects inside the analyzer [14,15]. Ph.D. theses and reports have examined several design trades [16,17] for RPAs, and the finite size of small RPAs have been shown to also cause errors in the measured IEDF [6]. Modeling is typically involved in the design of modern RPAs. Examples of modeling codes used include the PIC code MAGIC [18], electrostatic potential solvers like SIMION [19], and PIC-DSMC codes [20]. Analytic models of the space charge inside the analyzer are also useful for designing the aperture size and grid spacing in the RPA.

A. Modeling RPA Ion Trajectories

Modeling ion trajectories within the body of an RPA can guide design decisions of RPA geometry and grid structure. Studies have examined how RPA grid geometry and spacing affect grid and collector currents, identifying artifacts that arise with select grid configurations and geometries [21–23]. Ion trajectory simulations can be useful in determining whether a specific grid design or orientation is appropriate. As part of a diagnostic package, Huang et al. developed three RPA engineering design units (EDUs) with aligned grids and varying grid aperture sizes. Ion trajectory simulations were conducted for each design to gain a better understanding of ion physics within an RPA body. These simulations revealed the influence of the spatially varying electric fields within the RPA body on ion motion, explaining anomalies in ion behavior. The simulations also provided termination current data for individual grids, allowing simulated current as a function of voltage (I-V) traces to be generated [23]. The findings from Huang et al. contribute to a broader understanding of the tradeoffs associated with grid alignment. However, effects of unaligned and aligned grids have produced conflicting results showing both desirable and undesirable effects. While alignment provides greater grid transparency and therefore higher signal-to-noise ratio (SNR) [21,23], Trottenberg et al. demonstrated that alignment of the grids can lead to deviations from ideal RPA behavior, such as a peaking in

collector current just before the falloff of I-V trace [22]. These studies demonstrate the value of ion trajectory simulations and their ability to explore existing tradeoffs in the design of an RPA.

B. Recommendations for RPA design

The simplest design for an RPA is a just a biased collection plate to select the collected ions vs. energy; however, there are several issues with this setup, including the collection of electrons and secondary electron emission contributing to the overall collected current. The addition of grids in front of the collector can reduce these effects. The typical electrode configuration of an RPA, shown in Fig. 2, features four grids and each serves a specific purpose described in the following sections. Briefly, adding a floating grid (1) at the entrance to the RPA attenuates the plasma entering the probe to reduce internal space charge. An electron repelling grid (2) prevents the plasma electrons from entering the RPA. The ion discriminator grid (3) filters ions by kinetic energy before they are affected by the electron suppression grid. An electron suppression grid (4) diverts secondary electrons emitted when high energy ions impact the collector back to the collector.

1. Grid 1 – Floating Grid

The first grid facing the plasma is typically allowed to float relative to the plasma. This is intended to minimize perturbations of the plasma due to the presence of the analyzer. However, the sheath generated between the plasma and the first grid, so long as it is floating or biased near the plasma potential, provides all the isolation needed and the real purpose of first grid is to attenuate the plasma density and reduce the space charge effects inside the analyzer, which are discussed in detail in Section III.B.3. This enables finite grid aperture sizes and finite grid spacing to be used in applications where higher plasma densities exist. Therefore, the first floating grid is designed primarily for transparency to reduce the incident plasma density and ion flux on the following grids sufficiently for them to repel the electrons and discriminate the ions in the plasma.

2. Grid 2 – Electron Repelling Grid

The second grid is normally biased negatively relative to the incident plasma potential. The required bias depends on the incident plasma density, the grid aperture diameter and thickness, and the grid spacing relative to the other electrodes. The electron repelling grid aperture diameter and thickness must be selected such that incident plasma electrons are rejected. Similar techniques are used in the design of ion thruster grids to prevent electrons from the ion beam plasma from backstreaming into the positive potential thruster.

Any electron current that penetrates the electron repelling grid results from the tail of the Maxwellian electron distribution in the thruster beam overcoming the potential barrier that is established by the electron repelling grid aperture. The current of electrons into the ion discriminator and collector regions is determined from the random electron flux in the beam plasma multiplied by the Boltzmann factor for the potential difference between the incident plasma, V_i, which is often very close to the bulk plasma potential, and the minimum potential in the electron repelling grid region, V_m [24]:

$$I_e = \frac{1}{4} n_e e \left(\frac{8kT_e}{\pi m}\right)^{1/2} \exp\left(-\frac{V_i - V_m}{T_e}\right) A_a, \tag{2}$$

where I_e is the electron current inside the RPA, n_e is the electron number density, e is the charge of an electron, k is Boltzmann's constant, T_e is the electron temperature, m is the mass of an electron, and A_b is the cross-sectional area of the beamlet. The current of ions in the plasma flowing through the grid aperture, I_i, is

$$I_i = n_i e v_i A_a, \tag{3}$$

where n_i is the ion number density. The ion velocity through the system, v_i, is

$$v_i = \sqrt{\frac{2e(V_p - V_i)}{M}}, \tag{4}$$

where V_p is the local plasma potential and M is the mass of an ion. Combining Eq. (2) through Eq. (4), the minimum potential necessary to repel the plasma born electrons is

$$V_m = V_i + T_e \ln\left(\frac{2I_e}{I_i}\sqrt{\frac{\pi\, m}{M}\left(\frac{V_p - V_i}{T_e}\right)}\right). \tag{5}$$

Eq. (5) describes the required potential difference between the incident plasma potential on the RPA and the minimum potential inside the electron repelling grid aperture to produce a specified amount of penetrating electron current, I_e, relative to the ion current, I_i, flowing towards the collector. Note that this equation is independent of the grid geometry because it deals solely with the potential difference between a given value of the minimum potential, V_m, (independent of how that potential is produced) and the incident plasma potential, V_p.

The minimum potential within the grid aperture is determined by the grid geometry, the applied grid potentials, and the plasma space charge in the analyzer. The minimum potential in a grid aperture can be found without considering space charge effects by an analytic solution to Laplace's equation derived by Spangenberg [25] for thin grids in vacuum tubes. Spangenberg's expression was simplified by Williams [26] for most grid configurations to

$$V_m^* = V_a + \frac{d_a(V_p - V_a)}{2\pi x}\left[1 - \frac{2t_a}{d_a}\tan^{-1}\left(\frac{d_a}{2t_a}\right)\right] e^{-t_a/d_a}, \tag{6}$$

where V_m^* indicates the minimum potential from Eq. (5) with the plasma space charge neglected, V_a is the potential applied to the electron repelling grid, t_a is the repelling grid thickness x is the grid separation distance, and d_a is the electron repelling grid diameter. Eq. (6) provides the potential dependence on the geometry of the grids but is only useful if the beam space charge is negligible.

The reduction in the magnitude of the minimum in the aperture potential due to the presence of the ion space charge in the grid aperture can be calculated using the integral form of Gauss's Law:

$$\oint_S \mathbf{E} \cdot d\mathbf{A} = \frac{1}{\varepsilon_o}\int_V \rho \mathrm{dV}, \tag{7}$$

Where $\mathbf{E}$ is the electric field, $d\mathbf{A}$ is the differential surface area element, and ρ is the ion charge density within the Gaussian surface which has a surface area S and encloses volume V. Following the derivation detailed in Ref. [24], the potential difference between the aperture axis and the grid wall, ΔV, is

$$\Delta V = \frac{I_i}{4\pi\varepsilon_o v_i}. \tag{8}$$

where ε_o is the permittivity of free space. Since scalar potentials can be added, the sum of Eq. (5) and Eq. (8) gives the total of the potential minimum in the grid aperture as

$$V_m = V_a + \Delta V + \frac{d_a(V_i - V_a)}{2\pi x}\left[1 - \frac{2t_a}{d_a}\tan^{-1}\left(\frac{d_a}{2t_a}\right)\right] e^{-t_a/d_a}. \tag{9}$$

To calculate the electron current that penetrates the electron repelling grid as a function of grid voltage, Eq. (9) must be equated to Eq. (5) and solved for the electron to ion current ratio

$$\frac{I_e}{I_i} = \frac{e^{(V_a + \Delta V + (V_i - V_a)C^* - V_i)/T_e}}{2\sqrt{\frac{\pi m}{M}\frac{(V_p - V_i)}{T_e}}}, \tag{10}$$

where the geometric term C^* is given by

$$C^* = \frac{d_a}{2\pi x}\left[1 - \frac{2t_a}{d_a}\tan^{-1}\left(\frac{d_a}{2t_a}\right)\right]e^{-t_a/d_a}. \quad (11)$$

It is typical to set the electron to ion current ratio in Eq. (10) to a negligible level of about 1% and solve for the grid potential required to achieve that ratio for a given grid design and bias. An example of the electron current percentage as a function of electron repelling grid bias is shown in Figure 3 for the specific electron repelling grid design described in Ref. [27] that was used to analyze plasma with a density of $1x10^{17}$ m^3 and an electron temperature of 5 eV incident on the floating grid of the RPA. In this case, the potential of the discriminator grid (grid 3) was selected to be +100 V to produce the maximum potential depression expected in the electron repelling grid aperture. Thus, an electron repelling grid bias of -20 V is sufficient in this case to attenuate the electron current leakage to negligible levels.

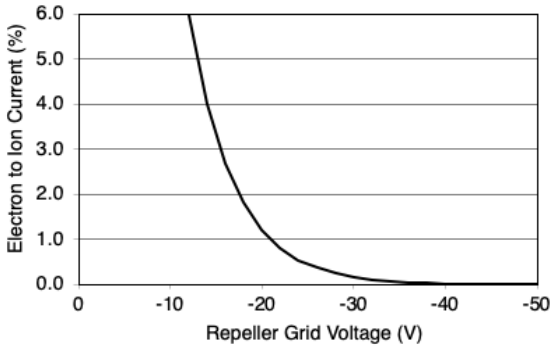

Figure 3. Percentage of electron to ion current flow thru the electron repelling grid as a function of repelling grid voltage showing the onset of electron leakage to the collector region as the repelling voltage is decreased).

3. Grid 3 – Ion Discriminator Grid

The ability of any RPA design to accurately measure the ion energy distribution function depends on the amount of space charge in the ion discriminator grid region. Historically, this has been analyzed by calculating the Debye length, λ_D, in this region of the analyzer. That parameter is then used to determine the spacing between the electron repelling and ion discriminating grids and to define the aperture sizes in the grids. According to the analyzer design process of Hutchinson [14], the diameter of the grid apertures should be less than the thickness of the plasma sheath in order to minimize the shielding effect of the grids by the plasma. Hutchinson derived a design relation for the spacing, *x*, between the electron repelling grid and the ion discriminator grid by equating the ion Bohm flux to Child Langmuir flux:

$$\frac{x}{\lambda_D} = 1.02\left(\frac{eV}{kT_e}\right)^{3/4}, \quad (12)$$

where *V* is the potential between the grids at which space charge effects are greatest. The spacing between each of the grids in the analyzer is usually selected to be as small as possible to eliminate space charge effects inside the analyzer that tend to artificially widen the ion distribution function while avoiding voltage breakdown. Analysis by Hutchinson [14] has been used [15] to design the maximum gap distance between RPA grids to avoid space charge effects, giving

$$x < 1.02\,\lambda_D\left[\left(V/T_e\right)^{1/2} - \frac{1}{\sqrt{2}}\right]^{1/2}\left[\left(V/T_e\right)^{1/2} + \sqrt{2}\right], \quad (13)$$

where *V* is the voltage difference between the grids and the electron temperature is in eV. The grid gap between the electron repelling and discriminator grids from Eq. (13) should be less than about four Debye lengths, a common range for a sheath thickness

$$d \lesssim 4\lambda_D \approx 3x10^4\sqrt{T_e/n_i}. \quad (14)$$

The value for the Debye length is often calculated incorrectly as the Debye length of the incident plasma; however, that plasma is modified at the electron repelling grid such that only ions penetrate toward the discriminator grid. Since there is no longer plasma in the grid gap and in the apertures of the discriminator grid, the physics used to derive the Debye length does not directly apply. An alternative analysis is required to correctly space the grids and choose the aperture sizes. To describe this further, consider plasma near the exit of a hollow cathode with an electron temperature of 5 eV and an ion number density of 10^{18} m^{-3}. This gives a grid gap of less than 0.05 mm, which is very small and typically requires MEMS fabrication techniques. However, since only ions penetrate the electron repelling grid, the ions in the gap after this grid have significant velocity (and lower density) because they were accelerated into the analyzer from the local plasma potential. This gives ions in this region an energy which is typically near the discharge voltage (~25 V for this cathode example) plus the repelling grid voltage (~20 V). Assuming ions incident on the RPA arriving from the previously described cathode plasma are accelerated past the repelling grid at ~45 V and attenuated by the floating and repelling grid transparencies, the ion number density term between the electron repelling and ion discriminator grids in Eq. (13) is reduced. Thus, the Debye length is increased such that the grid gap can be about 0.5 mm. Likewise, space charge effects are minimal in the gap between the discriminator and collector because at low discriminator voltage the ions have high velocity (lower density), and at high discriminator voltage the majority of the ions are repelled by the discriminator grid and the density of the slowed ions is reduced. Therefore, grid spacings on each side of the discriminator grid are generally approximately 0.5 mm for machining practicality and potential holdoff, which also can easily stand off the voltage applied between the grids.

Finally, due to the finite ion charge density inside the discriminator grid aperture, the potential on axis will be lower than the applied voltage and some ions will penetrate the discriminator grid and be collected that should have been repelled. This potential depression in the grid aperture was shown clearly in the thesis by Sullivan [19] where simulation of the ion trajectories near a grid aperture inside the RPA were performed using the program SIMION which calculates the electrostatic potential distribution for a given configuration in 2D and also simulates ion trajectories through the configuration. The analysis showed that this potential depression effect in the discriminator grid can cause a significant broadening of the IEDF calculation, as discussed in Section IV.F.1 This problem is solved by designing the ion discriminator using two grids connected electrically together as the discriminator grid or by using a single thicker grid [27]. The apertures for a double-grid discriminator can be aligned or not, as long as the grid gap between them is on the order of or less than the aperture diameter so that the potential between the grids everywhere is the same as the applied potential. Using a double-grid discriminator eliminates the potential depression problem and reduces broadening errors in the IEDF determination. However, the use of a double-grid discriminator will alter ion trajectories around the filter aperture. For an RPA with aligned grids, this may lead to greater impingement on the secondary electron suppression grid, requiring the size of the grid 4 apertures to be increased. This effect can be modeled in simulations, and the geometry of the grids can be re-designed to account for the effect.

4. Grid 4 – Secondary Electron Suppression Grid

Ions with energies greater than the applied discriminator grid voltage will fall to the collector and can strike it with significant energy. This has the potential to generate secondary electrons, which will be collected by the positively biased discriminator grid. Since emitted electrons are electrically the same as collected ions, secondary electron emission will distort the measured IEDF. A negatively biased 4th grid can be inserted between the ion discriminator grid and the collector, as shown in Fig. 2, to suppress the secondary electron emission and return it to the collector. Typical electron suppression grid biases are on the same order of magnitude as the electron repelling grid. The thickness of the electron suppression grid may also affect the measured IEDF [23]. Modeling has shown that as the retarding potential of the discriminator grid approaches the ion energy of the incident plasma and the axial velocity of the ions decreases, the ions begin to pick up a small amount of radial velocity that will rival the axial velocity due to the fact that the retarding field is not radially uniform. These radially diverted ions will likely hit the electron suppression grid, resulting in a broadening of the IEDF. However, it was found that this effect can be minimized by placing the electron suppression grid as close to the ion discriminator grid as possible, increasing the aperture size of the electron suppression grid so that it is larger than that of the ion discriminator grid, and making the electron suppression grid as thin as possible [23].

Collectors made of molybdenum, tungsten, and stainless steel have a secondary electron yield of less than 1% at ion energies <100 eV. In this case, the secondary electron suppression grid can be neglected, which can increase the net transparency of the grid system, enabling higher collector currents which reduces the SNR. This reasoning was applied in a study that used a stainless-steel collector in the RPA, where it was stated that the secondary electron emission in the RPA from ion bombardment of the stainless-steel surfaces was not a concern because the secondary electron yield due to Xe+ bombardment at energies below 1 keV is less than 0.02 electrons per ion [20].

5. Collector

The ion collector is usually a conducting flat disk or plate that collects the ions that passed through the grids within the RPA. Ideally, this will be the ions that passed through the discriminator grid. The collector should be made of a material with low secondary electron yield, such as most refractory metals. The use of such materials may eliminate the need for a secondary electron emission suppressor grid when the plasma energy is less than 100 eV. The use of materials with low secondary electron emission yield is suggested for all ion energies to reduce the effect.

6. RPA Assembly Summary

It should be noted that the multiple electrodes described in Sections III.B.1 – III.B.5 are not in fact absolutely necessary. A two electrode RPA can be constructed where the first electrode is the electron repelling grid and the second a biased collector. In this case, the repelling grid is directly exposed to the plasma without the attenuation of the floating grid, and so it is more difficult to achieve an aperture design that accomplishes electron rejection. Likewise, the bias on the collector is used to reflect and discriminate the ion energy without a separate grid. This necessitates making a low current measurement (typically ~1 μA) while varying the potential of the electrode within the dynamic environment of the discharge plasma without the benefit of the floating grid. All of this leads to problems with SNR. It is recommended to construct the RPA with the multiple grids described above in order to make the most accurate IEDF measurement.

7. Grid Construction

There are many considerations required for construction of the RPA grids discussed in previous sections, including grid material, aperture size, thickness, alignment, and effective field of view. In general, grids are constructed of a wire mesh or a stamped/perforated metal sheet. Grids should be made of a low sputter yield material such as stainless steel or refractory metals if required for higher temperatures or voltages. Mesh grids are simple and useful for higher plasma density applications because of their finite transparency that attenuates the plasma flux into the analyzer, thereby reducing space charge effects. However, mesh grids are difficult to align and will thus, decrease SNR in lower density systems. Electrodes with aligned stamped/perforated apertures can provide higher collector currents in lower density applications due to a net higher transparency for ion flow to the collector; although, these types of grids are more difficult to manufacture and require special fabrication and alignment techniques. Additional issues associated with grids that are not aligned include uncontrolled acceptance half-angles to the probe and lower energy resolution [23].

Grid thickness was briefly touched upon during the discussion of the electron repelling grid. When the grids are not aligned, the ion transparency decreases with increasing grid thickness [23], so thin grids are preferred for diagnostics with un-aligned grids.

8. Other Design Notes

If the application involves exposing the RPA to high energy plasma for prolonged periods of time, it may be necessary to place the RPA behind a protective cover and possibly deploy a shutter that only opens the analyzer entrance when data are being recorded. In such a case, the protective cover should be designed to conduct heat away from the vicinity of the RPA. The cover and shutter should be electrically configured to avoid impacting the trajectories of the ions entering the RPA. This is typically accomplished by either floating the cover and shutter or grounding them to the facility.

For operation with an RF thruster, the probe will have to have RF compensation. This is left to the user to research proper RF compensation methods based on the frequency at which the EP thruster is operating.

IV. Experimental Testing Methodology

The collection of filtered ion current collected at each of a wide range of retarding grid biases is ultimately processed to quantify (albeit with some limitations) the ion energy distribution function or IEDF. As EP thrusters are rich in temporal dynamics and turbulence, traditionally RPA raw data are heavily filtered to provide the time-averaged or bulk IEDF. Alternatively, time-resolved IEDF measurements may be attained using wideband transimpedance amplifier measured collector currents at an array of discrete retarding biases processed via a transfer function method originally pioneered for high-speed Langmuir probes by Lobbia [28], and later externed to laser induced fluorescence by Durot [29] and Chaplin [30] and RPA probes by Baird [31]. An additional method for fusing data obtained in the same manner is referred to as shadow manifold interpolation (SMI), and this has been implemented successfully to extract time resolved IEDFs from RPA data [31,32]. A typical RPA probe is operated via computer control to vary the retarding bias while simultaneously measuring both this bias and the collected ion current with options for voltage step sizes (or slew rates) and signal filtering. The recommended implementations of this test setup for RPAs in EP thruster discharges are outlined next.

A. Discriminator Grid Bias Sweep

As ion current measurements are needed at a wide range of filtering or retarding biases (from 0 V to 1.5x the discharge voltage with respect to facility ground is typical for HETs), a means to easily sweep this grid voltage is required. Benchtop DC power supplies, while simple, are not usually recommended due to their noise characteristics (often several volts peak to peak ripple) and un-needed current drive capability.[‡‡] The recommended approach is to utilize a source measurement unit (SMU) that can output a regulated precision voltage (with negligible ripple) across a large voltage range (typically ±1000 V) in a pre-programmable ramp or computer-controlled manner, such as the Keithley 2410 or 2470 units.

B. Electron Repelling and Suppression Grid Biases

One or more RPA grids are specifically used to repel electrons from the plume and secondary emission from the collector (due to ion collection bombardment). With a typical electron repelling bias of between -20 and -30 V, batteries are certainly a viable option but any linear DC power supply with moderate to low output ripple is recommended. While batteries may possess lower noise, a low-noise linear power supply is recommended due to the ability to readily vary the repelling bias, ensure reliable voltage output, and limit the supply current to prevent severe RPA damage in the event of a grid short.

An electron backstream study should be performed to confirm the selected electron repelling bias is sufficient. This study is performed by varying the electron repelling grid bias and biasing the ion discriminator to the maximum planned bias voltage while measuring the current collected by the ion discriminator grid. As the electron repelling grid bias increases, there will be a certain voltage, called the electron backstream limit, after which the collected current rises drastically. The electron repelling grid bias during actual testing should be selected to be at least $1 - 2\ T_e$ above this limit.

C. Time-Averaged Measurements

The minute bias-filtered ion currents collected by an RPA in an EP thruster plume are often measured in the range of fA/pA to uA/mA. These small current signals require specialized current measurement instruments and electrical setups. Measurement of the voltage drop across a resistive shunt is not recommended due to the large resistors that would be necessary along with their associated Johnson-Nyquist thermal noise; thus, a transimpedance amplifier (TIA) circuit or picoammeter instrument is required. The large dynamic range of the ion current across the swept range of filter biases, as large as six orders of magnitude, preferentially places auto- or variable-range electrometers/

[‡‡] DC power supplies that source up >600 V nearly all utilize switch-mode architectures that result in rather noisy output signals with several volts peak-to-peak ripple. However, DC supplies with linear architectures, four-quadrant current capability, or extensive output filtering can have suitably low output ripple (< 1 Volt peak-to-peak) and may then be used to sweep the retarding grid bias.

picoammeters or high-resolution (6+ digit) benchtop DMMs as the recommended approach for RPA current measurements. Common examples of these instruments are the Keithley 6400 series (fA to mA ranges), Keysight B2980 series (sub-fA to mA ranges) units, or Keithley DMM6500 (pA to A ranges). These instruments improve measurement fidelity and accuracy with various automatic zero-check and other internal compensations (e.g., AC power line cycle phase locked averaging). In some cases, the auto-ranging feature of these instruments can cause subtle glitches as the range changes (common if the unit is out of calibration). To still capitalize on the increased dynamic range of auto-ranging when glitches are occurring it is recommended to set a fixed input range at the start of the RPA bias sweep (at lowest discriminator bias which leads to highest ion collector current). Alternatively, multiple sweeps can be conducted with multiple fixed current measurement ranges and stitched together with overlap in post-processing. While discrete TIA circuits can be viable tools for the collection of ion current, they usually only have a single transimpedance gain and significantly less dynamic range (10^3:1 typical) compared to picoammeters (whose dynamic range with auto-ranging enabled exceeds 10^9:1).[§§] Note that the ion collector in a RPA is at a virtual ground bias which is effectively 0-V with respect to ground for the ions. If a precision DMM is used for current measurement then the "current in" connection would be the RPA collector while the "current out" would be shorted to the instrument ground—which must also be tied to the star ground of the test setup (e.g. vacuum facility walls and ground of other instruments).

Regardless of how the collector ion current is measured, the signal will undoubtably require filtering to enable the smooth 1st derivatives (dI/dV) needed to estimate the IEDF. This filtering is ideally conducted in the time-domain, namely many current and bias measurements collected at each discrete bias for a sufficiently long duration to produce a stable average. For example, dwelling at each bias voltage step for ~1 second and collecting raw data at 120 Hz would typically yield a stable average. Most picoammeters and DMMs automatically conduct averaging by simply setting the sample rate to a sufficiently low value (or large sample aperture or NPLC[***]) or by explicitly programming in a set number of samples to average (integration window). If the retarding bias is continually swept (no discrete voltage steps) then the slew rate should be sufficiently slow (a few volts per second or slower) to enable averaging of the collected data that do not span too large of a voltage so as to artificially broaden the voltage resolution and inadvertently filter or distort the true IEDF.

D. Time-Resolved Measurements

The setup and analysis for time-resolved RPA measurements are far more complex than for time-averaged RPA measurements but can provide unique insight into the transient ion dynamics of the EP discharge. While rapidly swept Langmuir probe measurements have been demonstrated in EP plumes [33], the rapid sweeping of RPAs has additional challenges (discussed later) and is not readily practical. Data fusion methods have been successfully used in conjunction with high-speed ion current measurements for reconstruction of time-resolved IEDFs. The data fusion methods will be discussed in Section V.B, while the requirements and methodologies for testing are presented here.

For this approach, a wideband TIA is required within close proximity (< 1 meter) to the RPA to limit the cable capacitance that would otherwise limit the TIA bandwidth to unacceptable levels. With large vacuum test facilities where the TIA must be located inside the vacuum chamber to limit cable capacitance, vacuum preparation of the TIA electronics is required. This can usually be achieved with suitable epoxy encapsulation of the circuit board in a metal enclosure. While pre-assembled TIAs are available (such as the Femto DHPCA-100), they are relatively economical and simple to assemble from a few elements as shown schematically in Figure 4.

It is recommended to verify the bandwidth of a given setup (including the same cable lengths as will be used for testing) since the stability and bandwidth are extremely sensitive to minute amounts of input capacitance. Indeed, the $C_{feedback}$ capacitor shown in Figure 4 is tuned or selected based on the input cable capacitance (1 m of RG-316 coax is ~90 pF). The output cable and DAQ are also included in this circuit model to simulate the output loading and stability. The main limitation of in-vacuum TIAs is that the transimpedance gain is fixed to a specific value which usually

[§§] Technically, it should be noted that picoammeters use an internal array of electronically switched TIAs, but their internal compensations, offset corrections, and autoranging make them ideal for RPA ion current collection.

[***] NPLC is common to Keithley instruments and stands for Number of Power Line Cycles the signal is averaged over to reduce the AC common mode noise.

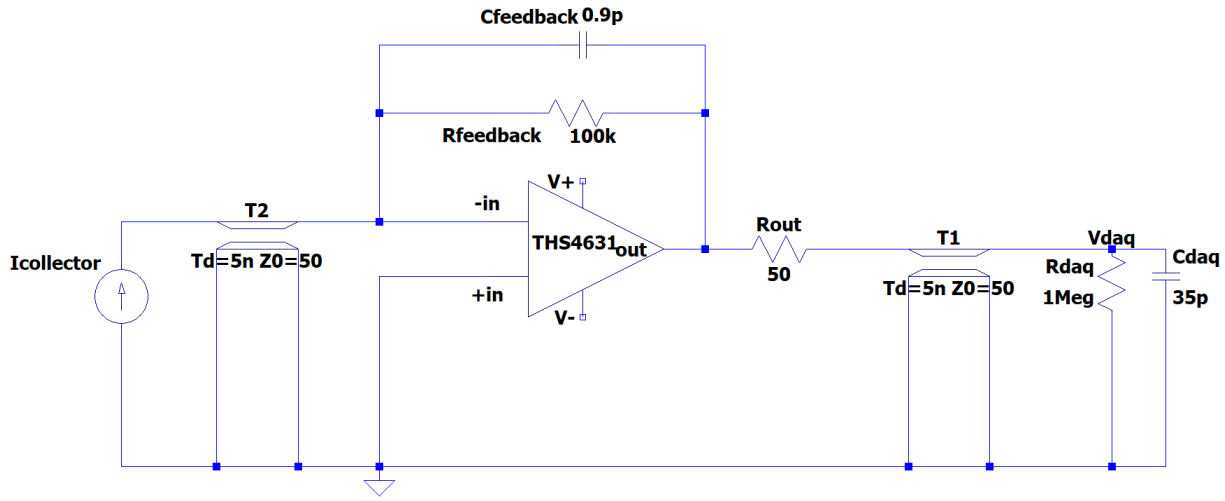

Figure 4. Basic TIA circuit suitable for transimpedance gain of 10^5 V/A with ~ 2 MHz bandwidth including 1-m coax cable from the RPA to the circuit input. Resistances are in Ω, capacitances are in F.

provides insufficient dynamic range to measure the ion collector current accurately at all retarding biases. This can be overcome by using 2 or more TIA circuits[†††] with different $R_{feedback}$ and $C_{feedback}$ elements and remotely switching the input connection via relays. The operation of a highspeed RPA also involves a suitably low-noise, high-speed, and high-resolution digitizer to sample, at a minimum, the collector current and a reference current. The reference current is used to reconstruct the temporally resolved I-V curve and IEDF.

The turbulent nature of EP discharges requires discrete sample sets typically well in excess of 1M samples to collect sufficient data to estimate the empirical transfer function [28] or perform the SMI reconstruction [31,32] with statistical invariance. It is recommended to utilize a PC with a multi-channel (synchronous) 16-bit discrete digitizing card, but newer 12-bit oscilloscopes with deep memory buffers may suffice at slightly reduced effectiveness (due to limited bit resolution or instantaneous dynamic range[‡‡‡]).

The operation of a time-resolved RPA can be a tedious manual process; thus, semi-automation of the setup is strongly recommended. Namely, a LabVIEW-, Python-, LabWindows-, or other software-based interface should be developed to step through a discrete list of retarding biases, set the proper instrument gains or ranges, trigger the digitizer, offload the high-speed buffers, save the raw binary data files with indexed file-naming, re-arm the digitizer, and repeat these steps for each of the retarding biases. With a bias step size of 2 volts, a 600-V RPA sweep would require at least 300 sets of high-speed digitizer data. For 10M point, 16-bit sample sets, this would require (300 biases) x (10^7) x (2 channels) x (2 bytes) = 12 GB for one RPA trace. Therefore, a PC with large storage capacity and RAM is required to save and process these data. The amount of data can be decreased if the user knows the approximate ion energy. The retarding bias steps can be selected to have a finer resolution near the expected ion energy, and a coarser step size in regions where no ion dynamics are expected.

E. Additional Setup and Operational Notes

As RPAs are typically operated directly on-axis of high-energy ion beams, the use of plasma resilient materials, thermal considerations, and health checks are recommended for reliable operation and data collection. While the electron repelling and suppression grids limit secondary electrons, the plasma ions outside and inside the RPA directly impact surfaces, transferring thermal energy to the probe and sputtering surfaces they impact. The sputtered material

[†††] Note that it may seem simpler use relays to switch the $R_{feedback}$ and $C_{feedback}$ for a fixed op-amp, but the relay or switch capacitance usually dwarfs the compensation $C_{feedback}$ and dramatically lowers the circuit bandwidth.
[‡‡‡] Since the input range of the digitizer or scope should be manually optimized for each retarding bias, the dynamic range can be larger than the raw digitizer bit depth.

may coat nearby surfaces, affecting probe measurements or causing electrical shorts. Selection of plasma wetted materials with low sputter-yields and shadow shielding of the grid and collector isolators is essential as well as occasional grid isolation of leakage checks. Namely, in addition to high-potential isolation verifications (using a Megger or similar instrument) for the matrix of 21 unique connections between the 4-grids, RPA body, collector, and facility ground, occasional full operation of the RPA in a non-plasma environmental state is recommended. These null state data provide baseline collector noise and ensure no internal shorts or conductive coatings on the isolators by ensuring no grid leakage currents exist.

While probe design with high-temperature rated materials is recommended, the use of polymer-based wire insulation fundamentally limits the upper allowed RPA temperature to the 200 – 400°C range. It is recommended to add a thermocouple or other temperature sensor to the RPA body to monitor the thermal state of the probe during experiments since the on-axis thermal flux from typical EP beams greatly exceeds the thermal steady state power that can be radiated in a typical ground test environment as seen in Figure 5. While placement of the RPA at a distance of 1 m or more away from an EP discharge does limit the plasma density and proportional thermal flux, typical EP ion beams > 300 eV present thermal fluxes that will still overheat RPAs dwelling in the primary beam too long, thereby requiring a motion stage to move the probe away from the plasma plume (recommended implementation), a shutter to shield the probe, or active thermal cooling.

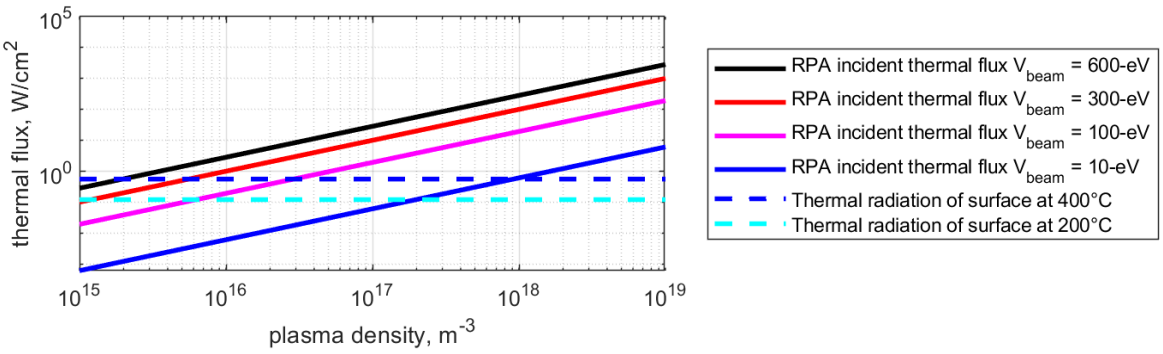

Figure 5. Approximate thermal flux for various beam energies and plume densities as well as thermal radiation estimates at 2 hypothetical RPA body upper temperatures demonstrating the need to limit the dwell time of RPAs at various locations within an EP discharge.

It is necessary to correct the measured ion energy obtained from the RPA by the plasma potential. This correction is discussed in Section V.A and Section V.C. There are several methods to obtain the plasma potential, and it is recommended that the reader consult Refs. [34,35].

F. Measurement Resolution Limits

Fundamentally, a given RPA geometry and the ambient plasma environment will impose limitations on the energy, temporal, and spatial resolutions of the diagnostic. Additionally, the precision of the sampling instruments can also limit the RPA resolution.

1. Potential Resolution

An RPA potential or ion energy resolution limit is set by the probe and grid geometry as well as the internal plasma density and temperature. While the grid design must ensure openings (wire radius, r_{grid}, and wire center separation, a_{grid}) and grid to grid separation (x_{grids}) fit within the parameters set in Section III.B, namely $\left(a_{grid} - 2r_{grid}\right)$ & $x_{grids} \lesssim 4\lambda_D$, these openings and gaps also must be sufficiently small to limit the electric field sag that leads to a variation in ion acceptance energies for a given retarding bias [36]:

$$\frac{\Delta V_{r,sag}}{V_r} = 1 - \frac{2\pi(x_{grid}/a_{grid}) - \ln(4)}{2\pi(x_{grid}/a_{grid}) - 2\ln[2\sin(\pi r_{grid}/a_{grid})]}. \quad (15)$$

where $\Delta V_{r,sag}$ is the maximum deviation or "sag" in the retarding grid potential that occurs at the center of the hole and V_r is the discriminator grid potential. For an arbitrary wire radius of 0.1 mm and ~40% transparency (or a_{grid} = 0.5 mm), a grid spacing of 1 to 10 mm provides a resolution limit of $\Delta V_{r,sag}/V_r$ = 9% to 0.9% respectively. In other words, at a beam energy of 600 V, the IEDF would broaden ~52 eV for the 1-mm grid spacing or ~5 eV for the 10-mm grid spacing.

In addition to field sagging, the RPA field-of-view half-angle, θ_{fov}, also invokes a resolution limit or broadening effect. Given that the distance between the inlet orifice of the RPA (of radius r_{inlet}) and the collector (of radius $r_{collector}$) is h_{RPA}, the field of view is

$$\theta_{fov} = \text{atan}\left[(r_{inlet} + r_{collector})/h_{RPA}\right]. \quad (16)$$

And since the grids maintain mostly axial electric repelling fields to the ions, the energy resolution is blurred or distorted by approximately the fraction shown in Eq. (17) [1].

$$\frac{\Delta V_{r,fov}}{V_r} = \sin^2\theta_{fov}. \quad (17)$$

For a typical RPA with a θ_{fov} = 14°, the field-of-view resolution limit is $\Delta V_{r,fov}/V_r$ = 6% or 35 eV for a 600 V beam, where $\Delta V_{r,fov}$ is the deviation in effective retarding potential from the field-of-view.

2. Temporal Resolution

The temporal resolution at which one may acquire an RPA IEDF is limited by instrument bandwidths as well as fundamental plasma response times. For the acquisition of time-resolved IEDFs via data fusion (e.g. transfer function method or SMI) from a non-rapidly swept RPA, the primary limits are the effective current collection instrument (TIA plus all cabling) and data acquisition system bandwidth as well as the natural ion plasma frequency[§§§].

Attempting to rapidly sweep the discriminator bias of an RPA introduces a host of addition temporal limitations akin to those seen in rapidly swept Langmuir probes [33]. Figure 6 shows limitations that arise from (a) the ion transit time through the RPA body and (b) the capacitive effects due to stray and sheath capacitances. An ion traveling through the body of an RPA experiences various electric fields due to the grid potentials. The impact on ion travel time is further discussed in Section V.B.4. The frequency limitation, *f*, as a result of these varying electric fields is approximated by

$$f = \frac{1}{t_{dwell,max} - t_{dwell,min}}, \quad (18)$$

where t_{dwell} is the dwell time of the ion inside the RPA body over all ion energies of interest. Above this limit ions of both high and low energies can reach the collector at the same time distorting the rapidly swept IEDF. This limit can be improved by decreasing the inter-grid spacing within the RPA. Capacitance of the internal sheaths as well grid electrodes also generate displacement currents, I_{disp}, that distort the energy-filtered collected ion current from rapidly swept RPAs.

$$I_{disp} = C\frac{dV}{dt} \quad (19)$$

[§§§] While the ions internal to an RPA are not a quasi-neutral plasma, the same theoretical natural mode as the ion plasma frequency is setup between the ions and the biased grids and surfaces.

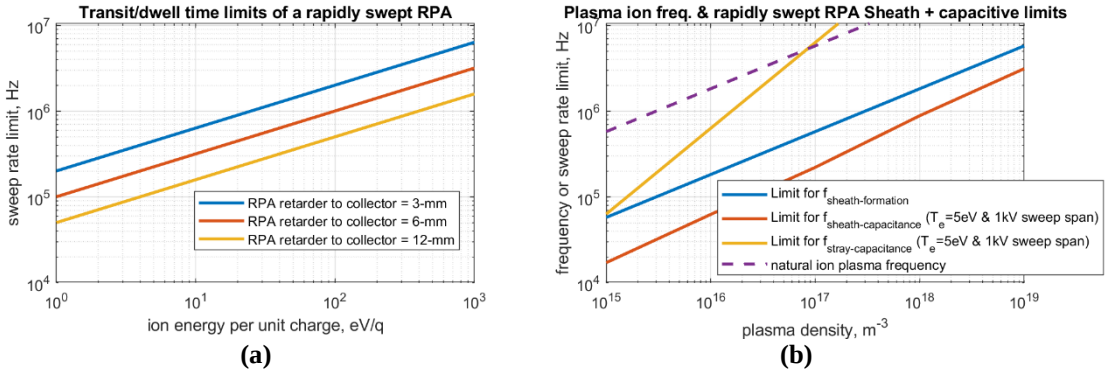

Figure 6. (a) Ion transit time per Eq. 30 and (b) sheath plus capacitance limits applicable only to rapidly swept RPAs for various discriminator biases and internal densities. The natural ion plasma frequency, (b) dashed-purple -line, is also shown which is a fundamental temporal limit for any time-resolved RPA analysis.

An additional limitation can be set up for RPAs with insulating (and unshielded) or electrically floating bodies that will couple to the local (and naturally oscillating) plasma floating potential and capacitively displace current from the collector—an issue easily remedied by grounding the RPA body.

3. Spatial and Angular Resolution

The spatial resolution is fundamentally limited by the local Debye length but in practice is set by the entrance aperture of the RPA which is generally 5 – 10 mm in diameter. The geometric field of view from Eq. 16 sets that approximate angular resolution of the cone within which ion trajectories can reach the collector. While it is plausible to design a narrow highly collimated RPA with a small field of view, alignment of the probe will become challenging due to the finite source size of the EP thruster, and the validity of using the generated IEDF data to evaluate estimated surface (spacecraft) interactions or sputtering is diminished (unless the probe is rotated through all possible incident angles to enable integration of the IEDF flux the exposed surface would see at that location). It is recommended that the field of view be sufficiently large to image an area at least 1-2 times the overall thruster diameter (for the RPA distance planned) to ensure that the vast majority of thruster emitted ions can reach the collector when the probe axis is pointed at the thruster center. For situations when the RPA cannot be pointed at the thruster center, or when there are significant off-axis ions, it is suggested the user consult Ref. [37] for suggestions on how to interpret the data. Caution needs to be used when RPAs are positioned far away from the thruster particularly when background pressure effects lead to CEX diffusion of the high energy ions to lower non-flight-like distributions.

V.Data Analysis

The level of RPA data analysis effort can vary with the application. For example, obtaining the average ion energy from the main beam for the purpose of calculating voltage utilization to support efficiency analysis only requires approximate ion energy distributions; whereas, predicting thruster-induced erosion of the spacecraft may require accurate ion energy distribution from the side plume region of the EP thruster. Calculating an accurate ion energy distribution typically requires in-depth knowledge of the sensor characteristics and additional data analysis steps. For more complex efforts, the user is advised to perform an exploratory activity to determine whether the selected approach needs to be refined before settling on a final analysis approach. Regardless of the selected approach, the user should try to estimate the uncertainty in the final results associated with the fidelity of the analysis performed.

A. Time-Averaged Analysis

Typical analysis of time-averaged RPA data starts with smoothing the collector current signal. This step is usually necessary because the next step involves performing a derivative on the signal. Filters that are appropriate for smoothing range from simple box-car averaging to a Savitzky-Golay filter [38,39]. In an HET application, it is not uncommon to need to apply smoothing twice. Note that each application of smoothing broadens any feature present

by an amount roughly equal to the characteristics span of the filter. Some exploration may be necessary to find the correct balance between achieving sufficient smoothing and avoiding excessive signal broadening for a given data set; therefore, we caution against excessive smoothing.

The next step is to perform the negative of the derivative of the smoothed collector current signal as a function of the bias voltage (I-V trace) as shown in Eq. (20) to get the IEDF,

$$J_{total} \equiv \int_0^{V_{max}} IEDF(V)dV. \tag{20}$$

where J is the current flux. Using the fact that the ion energy per charge, $\mathcal{E}$, is the difference between the retarding potential and the plasma potential and invoking the probability distribution function of the ion energy gives

$$1 \equiv \int_0^{\mathcal{E}_{max}} f_{pdf}(\mathcal{E})d\mathcal{E} \text{ with } f_{pdf}(\mathcal{E} = V - V_p) = \frac{dI_{collector}}{dV}\left[\int_0^{V_{max}} \left(\frac{dI_{collector}}{dV}\right) dV'\right]^{-1}. \tag{21}$$

Combining Eq. (20) and Eq. (21) results in

$$IEDF(\mathcal{E}) \equiv J_{total} f_{pdf}(\mathcal{E}), \tag{22}$$

which provides the IEDF in units of ion flux per electron volt directly from the experimental RPA measurements of the collector current at each discriminator bias. The total ion flux that occurs for $\mathcal{E}$ = 0, or when $V_{retarding} = V_{plasma}$, is

$$J_{total} = \frac{I_{collector}(V_{retarding}=V_{plasma})}{A_{inlet} t_a \Omega_{RPA}} = \frac{I_{collector}(V_{retarding}=V_{plasma})}{A_{inlet} F_{transmission}}, \tag{23}$$

where $\Omega_{RPA} = 1 - \cos(\theta_{fov})$ (maximum = 1) is the solid angle field of view and t_a is the effective grid transparency. Incorporating Eq. (23) into Eq. (22) gives,

$$IEDF(\mathcal{E} = V_{retarding} - V_{plasma}) = \frac{I_{collector}(V_{retarding}=V_{plasma})}{A_{inlet} t_a \Omega_{RPA}} \frac{dI_{collector}}{dV}\left[\int_0^{V_{max}} \left(\frac{dI_{collector}}{dV}\right) dV'\right]^{-1}. \tag{24}$$

The result of the derivative is proportional to the ion energy per charge distribution function, and, if dealing with a single ion species, proportional to the ion energy distribution function [14]. Note that in EP thruster applications, the plasma plume typically contains several multiply charged species, typically >20% for HETs, so that the ion energy per charge distribution is only approximately proportional to the ion energy distribution. The result shown in Eq. (24) is generally sufficient for simple RPA analysis, but there are a number of confounding factors that make this result a poor representation of the true ion energy distribution function, which will be explored in later sections.

1. Example Data Sets

Figure 7**Error! Reference source not found.** shows an example of raw data from an unaligned-grid RPA measuring the plume of a Hall thruster operating at 300 V, 6.25 kW, from a distance of 1.5 m while at 0 degrees from the firing axis along with the data reduced using Eq. (24) [40]. The angular positions of all data shown are measured with respect to the firing axis. In this example, the data were processed with no smoothing, with a Savitzky-Golay filter applied once to the raw data, and then with a Savitzky-Golay filter applied twice to the raw data.

Figure 8 shows reduced data from the same experiment with the thruster operating at 300 V, 6.25 kW, where the RPA was positioned at various angles from the firing axis [40]. This figure was plotted in semi-log scale to better highlight the variation in signal magnitude that may be encountered in an EP thruster experiment. Figure 9 shows data at the same angular positions for the thruster operating at 600 V, 12.5 kW [40]. In the plume of an HET, there is typically some angle at which the dominant ion population transitions from the beam energy population to some lower energy populations [8,41]. This transition point depends on thruster and operating condition, but the angle at which

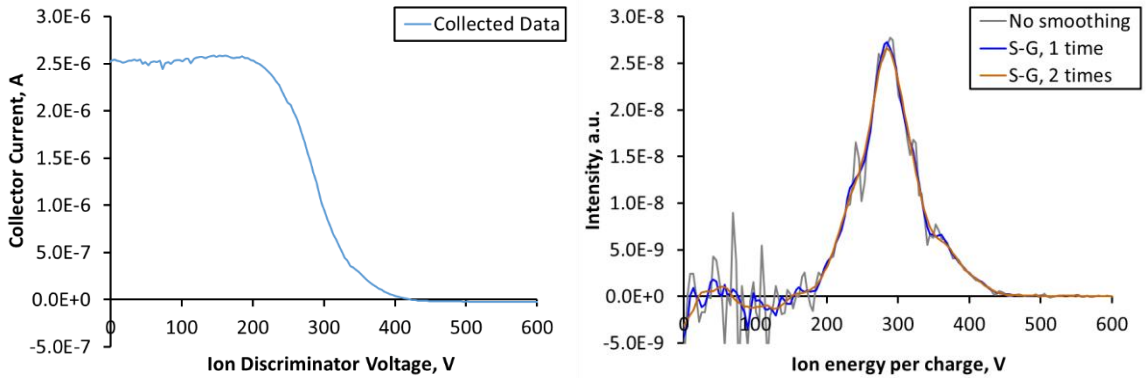

Figure 7. Left: Raw RPA data collected from an HET operating at 300 V, 6.25 kW; Right: processed RPA data with varying amounts of smoothing [40].

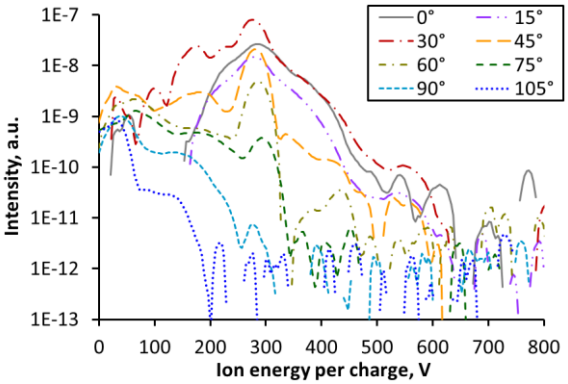

Figure 8. Example data set from a Hall thruster operating at 300 V, 6.25 kW [40].

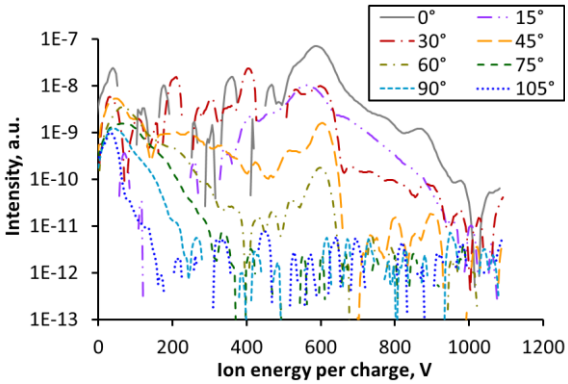

Figure 9. Example data set from a Hall thruster operating at 600 V, 12.5 kW [40].

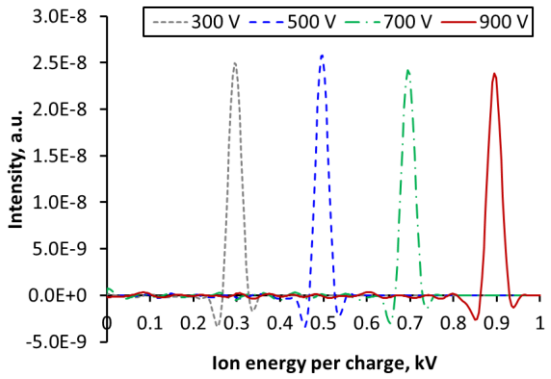

Figure 10. Example data from an ion source operating at varying beam voltage as measured by an unaligned-grid RPA [23].

the transition occurs tends to decrease with increasing discharge voltage. In the examples shown, the transition occurred between 60° and 75° when the thruster was operating at 300 V, 6.25 kW (Figure 8), and around 45° when the thruster was operating at 600 V, 12.5 kW (Figure 9).

Figure 10 shows an example of the data reduced using Eq. (24) from an RPA with the grids unaligned. The diagnostic is measuring the plume of an ion source operating at varying beam voltage at a distance of 450 mm directly downstream of the exit. The beam current was adjusted such that at this 450-mm-position, the current density was a constant at 0.2 A/m^2. An ion source is essentially an ion thruster that is optimized for good control of mono-energetic ion production as opposed to thrust production. It is worth noting that a separate test with an aligned-grid RPA with finer energy resolution in the same experimental setup demonstrated that the width of the ion energy distribution produced by this example ion source was narrower than the energy distribution measured with this example unaligned-grid RPA

[23]. Additionally, there are noticeable distortions in the energy distributions produced by this example unaligned-grid RPA, which are fairly common but typically go unnoticed in HET applications due to HET plume ions having broad energy distributions.

2. Computing Energy Statistics

The most common statistic extracted from RPA data is the averaged ion energy. These data are typically used to calculate the voltage utilization efficiency, $\eta_V = \langle \mathcal{E} \rangle / V_D$, which is a parameter used to assess how much of the discharge voltage is effectively applied to accelerate the ions [42]. For example, for an accelerating voltage of 300 V with an averaged ion energy of 290 eV, the voltage utilization efficiency is the ratio of the averaged ion energy to the acceleration voltage, in this case 0.967. In other words, 96.7% of the accelerating electric potential is effectively applied to accelerate the ions. Interestingly, the fact that RPA measures ion energy per charge instead of ion energy directly is advantageous for calculating voltage utilization efficiency as ion energy per charge correlates directly to the electric potential experienced by the ion, regardless of whether it is multiply charged.

The recommended approach to calculating the averaged ion energy is to calculate the first moment of the ion energy per charge distribution.

$$\langle \mathcal{E} \rangle = \frac{\int_0^{\mathcal{E}max} IEDF(\mathcal{E}) \mathcal{E} d\mathcal{E}}{\int_0^{\mathcal{E}max} IEDF(\mathcal{E}) d\mathcal{E}} \tag{25}$$

However, ion energy per charge distribution derived from RPA data can be susceptible to noise and distortions associated with non-optimal grid geometries. An example of distortion can be seen in the negative values on either side of each peak in Figure 9. These issues can be avoided by sampling a sufficient number of raw current and voltage points to permit a smooth derivate of the probe I-V characteristic and utilizing a grid design compliant with the recommendations in this work to minimize distortions

An alternative approach is to use the most probable ion energy as an approximation since it is typically within 10-20 eV of the averaged ion energy. Note that using the most probable ion energy only works well for reduced data that have been appropriately smoothed because the location corresponding to the most probable energy is easily shifted by noise spikes. Figure 11 shows an example of the analysis of RPA data from an HET operating at 200 V, 10 kW [12]. In this example, inadequate smoothing led to the most probable ion energy, as indicated by the black vertical dashed line in the bottom plot, being shifted to the right of the average energy of the distribution, as approximated by the red vertical solid line.

A third option for analysis of RPA data, called threshold-based averaging, is to take an in-between approach where only data above 50% of maximum is averaged. This approach is resistant to different forms of noise common to RPAs used in EP thruster applications. The drawback of this method is that it removes the signal caused by low intensity ion populations along with any low intensity grid-related distortions. Figure 11 illustrates threshold-based averaging with a 50 percent threshold. In the lower sub-plot of this figure, the red horizontal dashed line shows the intensity value corresponding to the 50 percent threshold and the red vertical solid line shows the result of averaging only the part of the ion energy distribution that exceeds the threshold. As this sub-plot

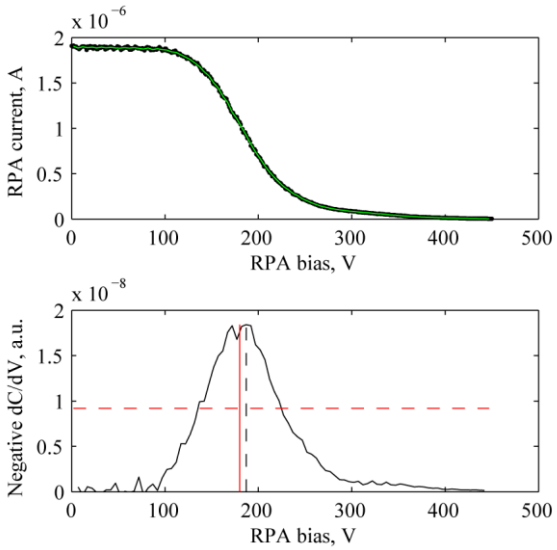

Figure 11. Example of RPA data analysis from an HET operating at 200 V, 10 kW [12]. Top: collector current plotted as a function of discriminator grid bias. Bottom: negative derivative of the collector current as a function of discriminator grid bias.

illustrates, threshold-based averaging left out contributions from the high energy tail, which may have been real ions and/or grid-related distortions.

3. Estimating the Ion Energy Distribution Function

Given the complexity of noise and distortions possible with an RPA, accurate measurements of the ion energy distribution function with an RPA typically require some preparatory work. An aligned-grid RPA will typically provide better results since they have finer energy resolution. Regardless of the choice of RPA, the transmission properties of the RPA should be characterized so that they can be corrected for during analysis. This characterization should determine the transmission coefficient of the RPA (i.e., how much of the ion current entering the RPA reaches the collector) as a function of input ion energy. It is recommended to use a Faraday probe to measure this current flux directly at the same location (using motion stages to exchange the Faraday and RPA probe positions). Alternatively, this can be attempted at an ion discriminator voltage of 0 V with respect to the local plasma potential. This transmission coefficient characterization is typically performed using an ion source because ion sources are optimized for controlling the characteristics of the ion beam. Figure 12 shows an example of the transmission coefficient of an aligned-grid RPA as a function of input ion energy. Once the transmission function is known, any distortion can be removed from the data produced by the associated RPA by dividing the data by the transmission coefficient.

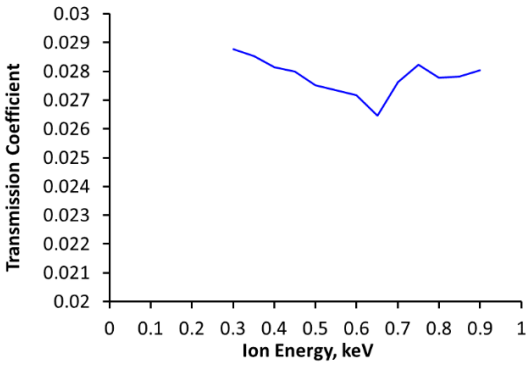

Figure 12. Example transmission coefficient as function of beam voltage for an aligned-grid RPA.

The response of an RPA can be distorted by grid impingement as described in the design section. If distortion cannot be eliminated by design, it may be possible to remove in post processing using deconvolution techniques commonly used in signal processing [43–45]. With that said, it is common in EP applications to treat this type of distortion as a factor that increases the measurement uncertainty. Figure 13 shows examples of minor distortions in the response of an aligned-grid RPA. In this example, the distortions appear as artificial low energy tails in the data corresponding to a roughly 2% reduction in the measured energy if one were to calculate the averaged energy.

Response of an RPA can also vary with input angle. Figure 14 shows an example of a study to characterize the transmission coefficient of the same RPA as a function of input angle. It is not recommended to correct RPA data if ions are entering at higher angles than the acceptance half-angle of an RPA. Instead, effort should be made to filter out ions that are entering at angles beyond the acceptance half-angle of an RPA. For example, a user with the RPA

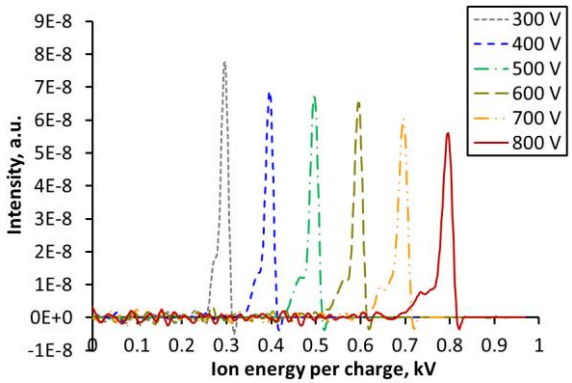

Figure 13. Example data from the transmission characterization of an aligned-grid RPA.

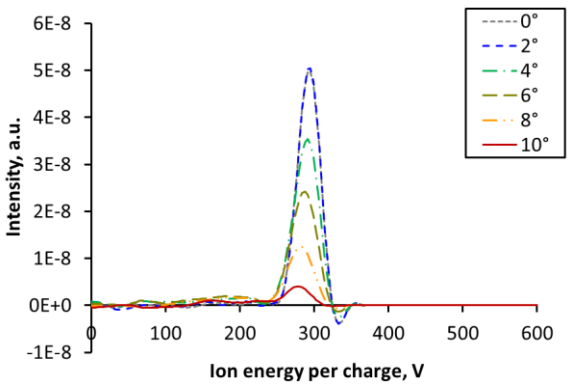

Figure 14. Example data from the characterization of an aligned-grid RPA for transmission versus input angle.

shown in Figure 14 may choose to filter out ions with an entrance collimator entering at angles beyond 4° to avoid the complex transmission coefficient function associated with ions entering at higher angles.

Alternately, the ion energy per charge distribution derived from Eq. (24) can be used as-is and an abbreviated characterization test can be performed to estimate the associated uncertainties. The user should estimate the level of uncertainties required by the application in question before attempting to remove any RPA-related distortions. For example, for the application of plume-induced wear associated with low energy ions, the total uncertainty tends to be dominated by uncertainty in the sputter yield and correcting distortions in the ion energy per charge distribution may not be necessary.

B. Time-Resolved Analysis

Several temporal analysis techniques exist to process time-resolved RPA data, all of which are used to align time-series signals. The chosen processing technique depends on the data collection methodology. Three techniques have routinely been found in literature: Data fusion, syncing/time-alignment, and fast sweeping. The goal of each technique is to form a time-resolved I-V trace and IEDF without corruption of the low-current signal. These techniques allow the time-resolved response to be observed, providing insight into the evolving ion dynamics within a plasma discharge. Each technique along with limitations to the analysis/measurement technique is discussed in the following sub-sections.

1. Data Fusion

Data fusion techniques facilitate the reconstruction of temporal datasets from single time-series, merging the data together as if the measurements were made concurrently. The data fusion reconstruction techniques commonly employed include the empirical transfer function (TF) method and shadow manifold interpolation (SMI). In studies of HETs the TF method has been a widely adopted approach for the reconstruction of spatiotemporal plasma properties [28–30,46–48]. While SMI has generally seen less use in EP applications, it has begun to receive increased attention in recent literature [31,32,49–52]. Once reconstruction of the time-series data is complete, time-resolved IEDFs can be obtained by differentiating the RPA collector current time-series with respect to the retarding potential for each instant in time. For brevity each of these methods are summarized below with several steps omitted. However, detailed explanations of the TF method can be found in the references listed above.

Transfer Function Method. The TF method employs the Fast Fourier Transform (FFT) to produce a transfer function relating an input and output time-series. The FFT algorithm transforms a finite length signal from time space into frequency space, allowing periodicities to be revealed. The dynamic behavior of the system is inferred by applying the FFT to simultaneously sampled input and output time-series, $X(t)$ and $Y(t)$, which represent a signal coupled to the plasma source, $I_{ref}(t,V_r)$, and the RPA collector current, $I_c(t,V_r)$, respectively. Each of these are recorded at a specified time and retarding potential. By taking the ratio of their Fourier coefficients, $A_y(k)$ and $A_x(k)$, a transfer function in the frequency domain, k, can be obtained.

$$\mathcal{H} = \frac{FFT[I_c(t,V_r)]}{FFT[I_{ref}(t,V_r)]} = \frac{A_y(k)}{A_x(k)}. \tag{26}$$

The newly formed transfer function relates the input and output signals and is used to obtain a synthetic reconstruction of the signal by multiplying the transfer function by a single common Fourier coefficient, $A_x^*(k)$

$$A_{y_{syn}}(k) = A_x^*(k) * \mathcal{H}(k). \tag{27}$$

By performing the inverse FFT, a synthetic time-series reconstruction, $y_{syn}(t)$ is obtained that is referenced to the common time-series. This process is repeated for each retarding potential at which data are sampled. The outcome is a set of RPA collector current time-series referenced to a common signal. The quality of the reconstruction depends on the selection of several parameters, including the sample depth, sample rate, the number of sets averaged, and FFT window averaging. This can possibly be performed spatially as well to create a spatiotemporal map of ion energy

distribution function. This would require temporal measurements as a function of retarding potential and *x*, *y* location in the plume. The locations would have to be mapped to the input signal.

Shadow Manifold Interpolation Method. A non-linear approach to temporal reconstruction is SMI, which relies on Takens' method of manifold reconstruction and convergent cross mapping (CCM) developed by Sugihara [53,54]. The reconstruction of temporal data can be achieved by creating shadow manifolds from time lagged samples of time-series data. SMI follows a similar process to CCM where the data are split into a training set and a test set. Given the time-series $X(t)$ and $Y(t)$, a training set, $x(t)$ and $y(t)$, and testing set, $\tilde{x}(t)$ and $\tilde{y}(t)$, can be established by splitting the time-series into two equal halves for each retarding potential. Just as with the TF method, series $X(t)$ and $Y(t)$ represent the coupled signal and RPA collector current, respectively. A time-lagged representation with embedding dimension E can then be constructed by forming an E-dimensional shadow manifold, M_x, using E time-delayed versions of the time-series $x(t)$

$$M_{x(t)} = [x(t), x(t-\tau), \ldots\ldots, x(t-(E-1)\tau)], \tag{28}$$

where τ is the time lag of $x(t)$ based on the number of samples. Shadow manifolds $M_{\tilde{x}}$, and M_y are of a similar form. A weighting function can be established based on a Euclidean distance metric, which finds the nearest neighbor(s), $\mathcal{N}$, in the shadow manifold $M_{x(t)}$ for each point in $M_{\tilde{x}(t)}$. The weighting function can then be used to estimate a reconstructed synthetic shadow manifold $\widehat{M}_{\tilde{y}(t)}$

$$\widehat{M}_{\tilde{y}(t)} = \sum_{i=1}^{N} w_i M_{y(t)}. \tag{29}$$

where w is the normalized weight. By projecting $\widehat{M}_{\tilde{y}(t)}$ back to one-dimension a reconstructed output signal $\tilde{y}_r(t)$ can be obtained. This process is carried out for every retarding potential until all RPA collector currents measurements have been reconstructed. Several parameters are important in the reconstruction process, including the training depth, E, τ, and $\mathcal{N}$.

Limitations to Data Fusion Analysis. Data fusion techniques can effectively reconstruct periodic signals, allowing ion energy dynamics to be studied; however, each method has limitations. In terms of data acquisition, the TF method requires a highly sampled data set, typically tens of MS; whereas, SMI can achieve a comparable reconstruction with only thousands of samples. Despite the need for a greater sample depth, the TF method is computationally more efficient, leading to shorter reconstruction times for equivalent data volumes. When reconstructing semi-aperiodic signals, SMI outperforms the TF method due to the linear and time-invariant nature of the TF method [49]. Nonetheless, for predominantly periodic signals, both data fusion techniques yield comparable reconstruction performance. Data fusion presents an effective technique to obtain time-resolved IEDFs but requires more complex algorithms to implement compared to alternative processing techniques. Additionally, these approaches have yet to be verified with an RPA for accurately reconstructing oscillation frequencies in 100 kHz and higher range, which includes oscillations such as axial transit time oscillations in HETs.

2. Time Alignment

The second analysis technique aligns oscillations in the collected ion current with a known reference signal. Once aligned, the collector current can be differentiated with respect to the retarding potential, allowing a time-resolved IEDF to be obtained. The exact methods for how signals are aligned differ and several methods have been attempted [55–58]. The basic principle behind time-alignment is to establish a reference signal that synchronizes with the RPA collector current signal. The reference signal chosen for alignment must be periodic in order to properly locate a common point in each sampled time-series from which the RPA collector current signal is aligned. For HETs, the reference signal is typically chosen to be the discharge current. Work completed by Delavière-Delion et al. applied a search algorithm to identify a common point, specifically the peak value of the discharge current, which is closest in time to the trigger point of the data acquisition system [55]. Additional steps are typically required to aid in the

identification of the common point within the reference signal such as averaging and filtering during both data acquisition and post-processing. With a reference signal established, the RPA collector current signal can be shifted in time to align with the reference signal. The alignment procedure would be repeated for all retarding potentials. Once alignment of all time-series is achieved, time-resolved IEDFs can be obtained.

Limitations to Time Alignment Analysis. A key limitation of the time-alignment technique is the challenge of accurately identifying a consistent point in the reference signal. While many thruster discharge oscillations are generally periodic, such as the breathing mode oscillation in HETs, their variability, or inherent turbulence, necessitates averaging the signal to isolate a repeatable feature. This averaging aids in the identification of a common point within the reference signal, but the signal is now distorted, obscuring the true ion energy dynamics. The averaging process significantly limits the time-alignment technique from capturing more irregular energy dynamics, such as axial transit time oscillations in HETs, which display more aperiodic behavior [59]. This approach also inherently assumes a temporal-phase ("transit time") linearity which is strictly invalid in any non-mono-energetic plasma beam since different ion energy populations propagate at different speeds.

3. Fast Sweeping

The fast-sweeping technique, in which the retarding grid of an RPA is swept at rates greater than the ion energy dynamics of interest to obtain time-resolved measurements has not yet been applied to an electric propulsion thruster. However, it is briefly mentioned here, as limited measurements have been made in a low energy tokamak edge plasma [60]. To enable measurements without significant distortion of the low collector current signal due to capacitive effects, the fast-sweeping RPA utilizes capacitance compensation circuitry. As the sweeping of the retarding grid and the sampling of collector current are made at high rates there is no need for temporal reconstruction of collector current time-series. Post-processing of the fast-sweeping measurements only requires the chopping the data to form discrete I-V traces representing an instant in time. Once the traces have been discretized, they can simply be differentiated to obtain the time-resolved IEDFs.

Limitations to Fast Sweeping Analysis. The major limitation of the fast-sweeping technique are capacitive distortions. To date, time-resolved RPA measurements using this technique have only been conducted with retarding grid sweep rates up to 30 kHz [60]. The other techniques described above are not susceptible to capacitive effects with increasing frequency. While capacitive compensation circuitry can be used to prevent some of the I-V distortion, the internal sheath capacitance is not directly able to be deconvolved due to it being a function of both the discriminator bias and internal ion density.

4. Time of Flight Correction

A time-delay correction must be applied to time-resolved IEDFs, to account for the time-of-flight of an ion from the thruster exit to the RPA collector. Assuming ions are at their final velocity as they leave the thruster exit plane, the time required for an ion filtered by a retarding grid bias of V_r to reach the RPA, t_{tof}, can be expressed as

$$t_{tof} = d\sqrt{\frac{M}{2ZeV_r}} \tag{30}$$

where d is the distance between the thruster exit and the RPA entrance, and Z is the charge state of the ion. Assuming only singly charged ions, $Z = 1$, this simple expression allows a basic correction to be applied to the IEDFs; although, the actual time of flight is more complex due to effects such as collisions and electromagnetic fields present in the thruster plume. This delay must be estimated and a correction factor applied for each energy level within the IEDF to account for the different velocities at different energies. An additional delay exists due to the finite time it takes an ion to travel through the body of the RPA. This delay is not simply the travel time through the length of the RPA body as the finite electric fields within the RPA influence the ion motion. The dwell time of an ion, t_{dwell}, can be described as a piece-wise function of the RPA characteristic length, ion velocity, and grid potential profile. By integrating the magnetic-field-free Lorentz force equation over the length of each potential profile for a given grid segment and

treating the potential profiles within the RPA as perfect parallel plate potential profiles for only singly charged ions, the dwell time of an ion can be estimated by solving the kinematic relation:

$$0 = \left(-\frac{eV_r}{2Mx_{grids}}\right)t_{dwell}^2 + \sqrt{\frac{2eV_{ion}}{m_i}}t_{dwell} - x_{grids} \tag{31}$$

As the retarding grid potential is increased, the dwell time of an ion with potential, V_{ion} will increase as well. Once the potential energy of the retarding grid exceeds the kinetic energy of the incident ion, the ion will no longer reach the collector. For ions which have the energy to overcome the retarding potential, the dwell time within the RPA is typically negligible compared to the time-of-flight from the thruster exit plane and can be neglected in most cases.

5. Example Data Sets

The techniques discussed above enable time-series data obtained with an RPA to be used for computing time-resolved IEDFs. As discussed, time-series data must first be reconstructed before time-resolved I-V curves can be processed, excluding the fast-sweeping technique which does not require temporal reconstruction. Figure 15 shows three RPA collector current traces before and after temporal alignment at three retarding grid potentials: 0 V, 10 V, and 100 V. Data fusion techniques were used to produce the results shown in Figure 15. Temporal reconstruction enables the time-series data to be synced allowing time-resolved I-V traces to be assembled and time-resolved IEDFs to be calculated.

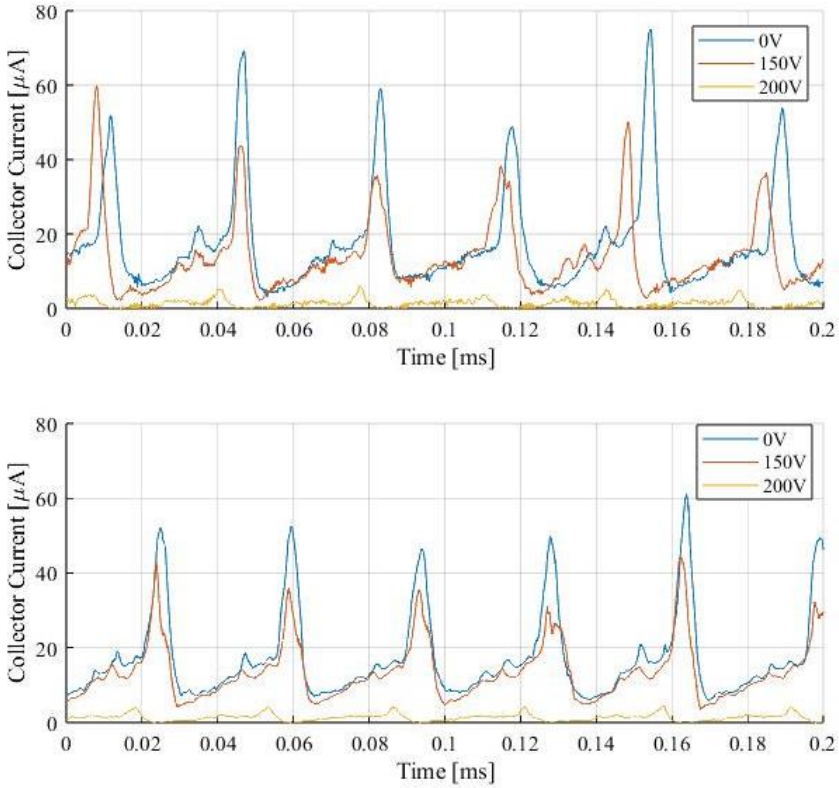

Figure 15. RPA collector current time-series before reconstruction (top) and after reconstruction (bottom).

Figure 16**Error! Reference source not found.** shows I-V traces and the corresponding IEDFs after temporal realignment from RPA data measured in the plume of an HET operating at 200 V, 200 W for five discrete time steps, along with the respective discharge current measurement for each I-V trace and IEDF. Discretizing the I-V traces and

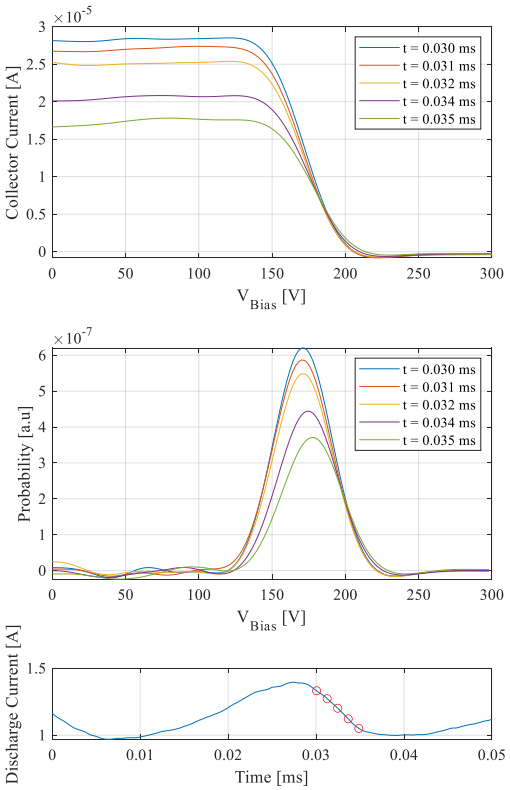

Figure 16. Discrete RPA I-V traces (top), IEDFs (middle), and associated HET discharge current indicated by the circles (bottom).

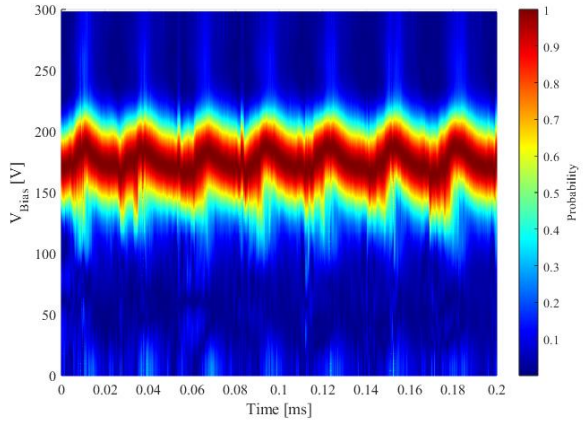

Figure 17. Time-resolved IEDF contour plot.

IEDFs, allows us to visualize changes in temporal ion energy from the perspective of a time-averaged measurement. To represent these data in three dimensions, a contour plot can be constructed, with the probability plotted on the z-axis and ion energy or time plotted on either the x or y axis. An example of such a plot is shown in Figure 17, where ion energy can be observed oscillating in time.

C. Correction Factors

In most EP thruster applications involving the RPA, the retarding potential must be corrected for local plasma potential. This is because most retarding grid biases are applied with respect to facility ground and the plasma plume around the RPA is typically elevated between 5 V and 15 V relative to the facility ground, assuming the wall of the facility is at ground potential. For this reason, the retarding potential experienced by ions entering the RPA is equal to the discriminator grid bias relative to the facility ground minus the local plasma potential at the entrance of the RPA relative to the facility ground. The local plasma potential at the entrance of the RPA can be measured with a Langmuir probe or emissive probe. It is also possible to simply bias the entrance grid of the RPA as if it were a Langmuir probe to find the plasma potential so long as the RPA entrance grid has the proper electrical connections.

Another correction factor that is sometimes considered is the charge-exchange (CEX) effect. The CEX effect tends to attenuate ions of different energy by different amounts. For xenon propellant, the methodology outlined in Shastry, et al. can be followed [61]. Note that Shastry, et al. describe how to correct ExB probe data for CEX effects, but the method is equally applicable to RPA data. For applications focused on finding the averaged ion energy for efficiency analysis, CEX correction is typically not necessary as the change in averaged ion energy with CEX effects is often negligible. Figure 18 shows the ion energy per charge profiles derived from RPA data in a background pressure effect study for an HET operating at 300 V, 9.4 kW with the RPA positioned at 90° from the firing axis [62]. In this study, the background pressure near the thruster ranged from 6 to 18 μTorr where operating condition "P1X" occurred at the lowest achieved background pressure of 6 μTorr and operating condition "PnX" denotes operation at n times the lowest achieved background pressure. Notably, while the amount of beam energy ions versus low energy ions changed significantly with varying background pressure (i.e., varying the amount of the CEX effect), the averaged energy of just beam ions, $\mathcal{E} \in [250\ eV, 350\ eV]$,

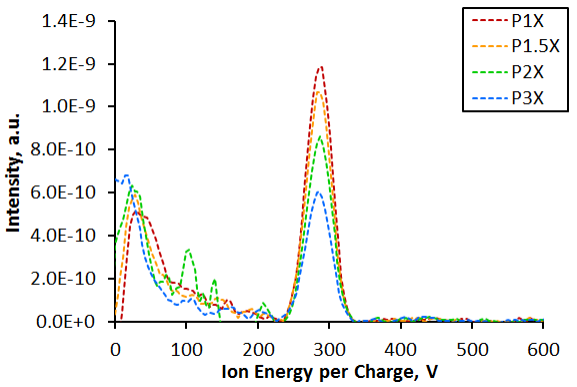

Figure 18. Examples of the ion energy per charge distributions at various background pressures for a Hall thruster operating at 300 V, 9.4 kW measured at 90° from the firing axis [62]. This figure is reproduced with the author's permission.

varied by no more than 1%.[****] The CEX effect will worsen with background pressure and experiments in high background pressure facilities may require CEX correction.

In applications involving characterizing plume-induced wear, analytical corrections for CEX may not be possible. This is because the thruster generates a neutral flow field that is present in flight that must be accounted for. Any analytical model that completely removes CEX effects may remove the effect associated with the thruster neutral flow field as well. Instead, the recommendation is to perform measurements at varying background pressure and use extrapolation to determine the parameter of interest at zero background pressure.

As previously alluded to, RPAs measure ion energy per charge distribution function, which is not exactly the same as the ion energy distribution function. To convert an ion energy per charge distribution function to an ion energy distribution function for a plasma with multiply charged species, one must multiply the ion energy per charge (x-axis in most of the figures presented) by the value of the ion's charge. If the plasma plume of interest contains a large amount of multiply charged ions in addition to singly charged ions, the RPA will measure an amalgam of energy distribution functions. Multiply charged ions also disproportionately contribute to the RPA derivative by the square of the charge state. It is not generally possible to determine how much of the measured distribution can be attributed to each charge species in post processing. If presence of multiply charged ions are suspected to be affecting the results in a non-negligible manner, the recommendation is to assess the situation with another diagnostic, such as an ExB probe (a.k.a. Wien filter spectrometer) [11] or an EVADER probe [13]. Alternately, the user can perform worse case analysis to determine how much uncertainty is introduced by assuming the RPA results are representative of all charged species present.

D. Uncertainty Analysis

When computing energy statistics such as the average ion energy, the dominant source of uncertainty typically comes from the data analysis approach. It is recommended that extra data sets are obtained for the purpose of assessing noise. For example, the user can take an additional 10 RPA I-V traces at a particular standard operating condition and representative location during testing and study how the extracted statistics vary over the 10 traces. There are also assessment approaches specific to data analysis techniques. For example, if the chosen approach is to average over the entire RPA trace, then one could vary the integration boundaries and assess how sensitive the results are to the boundaries. High sensitivity (averaged ion energy varying by more than a few eV) would imply there is a large amount of noise impacting the results. If the chosen approach is to use the most probable ion energy, one could look at how this most probable ion energy varies across the sample of 10 RPA traces. If the chosen approach is threshold-based averaging, one can look at the sensitivity of the results to the value of the threshold. The goal of this activity is to provide a data-driven assessment of how much measurement uncertainty is contributed by the chosen analysis approach and smoothing parameters.

Standard statistical methods can be applied to calculate the associated uncertainty at the chosen confidence level. For example, one can calculate the standard deviation from the 10 RPA traces and express the uncertainty as two times the standard deviation, corresponding roughly to a 95% statistical confidence. For more information on general uncertainty analysis and error propagation, see Dunn and Davis [63]. The amount of uncertainty contributed by the analysis approach is typically in the range of 1% to 15% of the accelerating potential depending on the sensor grid

[****] It should be noted that the overall average ion energies, $\langle \mathcal{E} \rangle$, of these distributions are altered significantly as the pressure is varied.

geometry and analysis method [23]. In contrast, modern electronics can easily achieve 0.1 V or better measurement resolution.

When estimating ion energy distribution functions, the accuracy with which collector current is measured becomes an important source of uncertainty. For example, when trying to measure the width of the ion energy distribution function with a low SNR, the noise in the collector current signal can have an outsized influence on the measured width. Sensor characteristics such as grid-related distortions and finite energy resolution of the RPA must all be accounted for. In each case, a dedicated study may be necessary to determine the amount of measurement uncertainty associated with each factor. For example, an additional 10 RPA traces at a particular standard operating condition and representative location can be recorded to enable an assessment of how the width of the ion energy distribution varies from trace to trace. Factors such as grid-related distortions can be assessed with an ion source with a known acceleration potential in a transmission coefficient characterization as illustrated in Figure 13 and Figure 14.

Although uncertainty contributed by the electronics are typically not drivers of the total measurement uncertainty, the user should assess the contributions by the electronics to be certain. This can typically be accomplished by examining the manufacturing specifications for the data electronics. Any custom circuitry may increase uncertainty contributions by the measurement electronics and should be assessed.

VI. Alternative Measurements Using an RPA

By applying potentials to the grids in different ways than have been described in Sections III and IV or by knowing further information about the probe, an RPA can be used to measure properties other than the ion energy. For example, an RPA can measure current density so long as the grid transmission efficiency is known. This information can be obtained readily with a Faraday probe or through ion trajectory simulations. One such study focused on the on the influence of grid alignment and ion energy effects on the transmission efficiency [64]. The results showed that when the grids are well aligned and ion energies exceed 100 eV, the transmission efficiency is equivalent to the optical transmission. However, at lower energies, less than 20 eV, the electric fields within the body of the RPA significantly influence ion trajectories. Grid misalignment further reduces transmission efficiency and field of view to the collector. Given an accurate estimation of RPA grid transmission efficiency, RPAs can provide a reliable ion current density measurement extending their effective use.

The plasma potential can be measured directly with the RPA so long as the first grid is connected to an appropriate power supply and current measurement device that can be isolated during desired ion energy measurements. In this manner, a separate Langmuir probe or emissive probe is not necessary to make the plasma potential measurements that are a necessary correction factor for IEDF data. This would be most simply done by operating the first grid as a Langmuir probe using analysis techniques presented by Lobbia and Beal [34]. The Langmuir probe can also provide data to calculate electron temperature, electron energy distribution function, electron and ion number density, and floating potential.

Another measurement that can be made with the geometry of an RPA is secondary electron emission, from which secondary electron emission coefficients can be determined. When a high-energy ion strikes a surface, it may cause a free electron to be emitted from that surface. Knowledge of the rate of secondary electron emission as a function of ion energy and surface material is necessary for plasma models, and specifically the design of RF plasma reactors [9]. Recall the current signal observed at the RPA collector consists of potential distributions inside the analyzer of an ion component due to incoming ions and an electron component due to secondary electrons that may escape from the collector in a direction opposite to ion movement. When the secondary electrons are hindered from escaping towards the plasma, and are rejected to the collector, the number of ejected and received electrons per time and surface unit is equal, ruling out the electron component of the collector current. This is the purpose of the electron suppression grid and necessary for measuring accurate IEDFs at ion energies > 100 eV. However, the device can be configured to quantify the electron component from secondary electron emission of the collector material. To do this, the RPA must be configured in such a manner that it can measure the collector current (1) when the secondary electrons are allowed to escape, thus contributing to the measured current and (2) when the secondary electrons are returned back to the collector and do not contribute to the measured current. This is done by either removing the electron suppression grid (grid 3) or by biasing the ion discriminator grid (grid 2) together with the electron suppression grid. The discriminator grid potential is then swept from a value that is negative with respect to the collector to a value that is positive with

respect to the collector. When the retarding potential is negative, the grid will act as an electron suppression grid and the collected current will be only from the ions. As the potential increases, the electron suppression will no longer be sufficient, and the measured current will be a contribution of both the collected ions and the secondary electrons. More details and analysis of this method are found in Bohm and Perrin [9].

VII. Conclusion

This paper presents guidelines and recommendations for the use of an RPA for ion energy analysis in EP thrusters. Measurement techniques and data analysis methods for both time-averaged and time-resolved measurements are discussed. Much of the discussion in these guidelines centers around the use of RPAs in HETs because HETs are the most prolific EP thruster in use and have complicated and rich ion dynamics. However, the measurement techniques and recommendations in these guidelines are applicable to other EP devices so long as the user accounts for the plasma conditions in the probe design. Advances in high-speed diagnostics and data fusion techniques are allowing RPA probes to be used to understand the complicated ion dynamics in EP thrusters. Energy measurements in the side plume of an HET may lead to further understanding of erosion mechanisms on the poles in magnetically shielded HETs. Uncertainty in the measurements from RPA probes generally result from grid alignment/design issues and SNR. Further uncertainty arises in the data reconstruction process for FT, SMI, and time alignment analysis methods. The presentation of these guidelines will enhance comparison of EP thruster operation between facilities and amongst different thrusters. This will improve measurement fidelity and increase the predictive capabilities of models for on-orbit thruster operations. The Appendix summarizes the recommendations presented in these guidelines.

Appendix: Summary of RPA Recommended Practices

Table A1 Summary of RPA probe guidelines and recommendations

Experimental Parameter/ Paper location	Guideline/Recommendation
Grid assembly/ III.B	1) Four-grid-design recommended for multi-purpose 2) Electron suppression grid may be eliminated for ion energies < 100 eV with appropriated collector material 3) two-grid discriminator combination recommended for highest accuracy of IEDF
Grid/collector material/ III.B.7	Low sputter yield and SEE material wherever possible
Grid alignment/ III.B.7	1) For higher SNR, grids should be aligned 2) If grids are thin, grid alignment is not as important
Grid thickness/ III.B.7	1) Thin as possible without sacrificing structural integrity
Grid spacing/ III.B.3, III.B.7	1) Distance between electron repelling and ion discriminator grids should be ~$4\lambda_D$ 2) λ_D should be calculated from ion number density and velocity between electron repelling and ion discriminator grids 3) Electron suppression grid, if included, should be as close to the ion discriminator grid as possible
Collector material/ III.B.5	1) Collector should be constructed of low sputter-yield material such as a refractory metal or non-magnetic stainless steel
Grid potentials/ III.B	1) Floating grid – floating 2) Electron repelling grid – perform a study to determine the appropriate value 3) Ion discriminator grid – from 0 V to about 1.5x the expected ion energy 4) Electron suppression grid – on the order of the electron repelling grid
Collector potential/ III.B.5	Grounded
Time resolved sample depth	10 – 50 MS (dependent upon data collection/analysis method)
RPA body electrical configuration	Ground RPA body

Correction factors	1) Correct for local plasma potential 2) If measuring for spacecraft interaction and operating pressure exceeds 10 uTorr, perform CEX correction or perform measurements at multiple background pressure
Diagnostic alignment	Aligned such that ions enter at 0 degree with respect to the entrance axis of the probe
Probe cabling	1) Use vacuum compatible, well-shielded cable 2) Use high temperature cable if cable heating is expected
Probe checkout	1) Check for electrical continuity from all electrodes to their respective connector pin; check for electrical isolation between electrodes and chassis 2) If leakage current detected, check for deposition on insulator between electrodes
Background pressure	If background pressure is greater than 10 micro-Torr, determine whether correction is needed or consider collecting data at multiple background pressures.

Funding Sources

This work was partially funded by the NASA Joint Advanced Propulsion Institute under grant number 80NSSC21K1118.

References

[1] Simpson, J. A., "Design of Retarding Field Energy Analyzers," *Review of Scientific Instruments*, Vol. 32, No. 12, pp. 1283–1293, Dec. 1961, doi: 10.1063/1.1717235.

[2] Sakai, Y. and Katsumata, I., "An Energy Resolution Formula of a Three Plane Grids Retarding Field Energy Analyzer," *Jpn J Appl Phys*, Vol. 24, No. 3R, pp. 337–341, Mar. 1985, doi: 10.1143/JJAP.24.337/XML.

[3] McCarrick, M. J., Ellis, R. F., Koepke, M., and Majeski, R. P., "Perpendicular Ion Energy Analyzer for Hot-ion Plasmas," *Review of Scientific Instruments*, Vol. 56, No. 7, pp. 1463–1464, Jul. 1985, doi: 10.1063/1.1138533.

[4] Molvik, A. W., "Large Acceptance Angle Retarding-potential Analyzers," *Review of Scientific Instruments*, Vol. 52, No. 5, pp. 704–711, May 1981, doi: 10.1063/1.1136655.

[5] Küdyan, H. M., "Interpretation of Electrostatic Energy Analyzer Data of a Flowing Plasma," *Review of Scientific Instruments*, Vol. 49, No. 1, pp. 8–10, Jan. 1978, doi: 10.1063/1.1135262.

[6] DeNeef, C. P. and Theiss, A. J., "Effect of Finite Analyzer Size on the Distribution Functions Measured in Field-free Plasmas," *Review of Scientific Instruments*, Vol. 50, No. 3, pp. 378–381, Mar. 1979, doi: 10.1063/1.1135832.

[7] Neiswender, D. D. and Kohout, F. C., "An Apparatus for Electron Energy Analysis in Glow Discharge Plasmas," *Review of Scientific Instruments*, Vol. 43, No. 10, pp. 1475–1480, Oct. 1972, doi: 10.1063/1.1685468.

[8] W. Huang and H. Kamhawi, "The Side Plume of Magnetically Shielded Hall Thrusters," *37th International Electric Propulsion Conference*, 2022-402, Cambridge, MA, Jun. 2022.

[9] Bohm, C. and Perrin, J., "Retarding-Field Analyzer for Measurements of Ion Energy Distributions and Secondary Electron Emission Coefficients in Low-Pressure Radio Frequency Discharges," *Review of Scientific Instruments*, Vol. 64, No. 1, pp. 31–44, Jan. 1993, doi: 10.1063/1.1144398.

[10] Yim, J. T., "A Survey of Xenon Ion Sputter Yield Data and Fits Relevant to Electric Propulsion Spacecraft Integration," *35th International Electric Propulsion Conference*, 2017-060, Atlanta, GA, 2017.

[11] Rovey, J. L., Toyofumi, Y., Huang, W., Thomas, R. E., Hurley, W. J., Farnell, S. C., Thompson, S. J., Farnell, C. C., Farnell, C. C., Brabston, W. P., and Young, J. A., "Recommended Practice for Use of ExB Probes in Electric Propulsion Testing," *39th International Electric Propulsion Conference*, 2025-483, London, UK, Sep. 2025.

[12] W. Huang, R. Shastry, G. C. Soulas, and H. Kamhawi, "Farfield Plume Measurement and Analysis on the NASA-300M," *60th Joint Army-Navy-NASA-Air Force Propulsion Meeting*, Colorado Springs, CO, Apr. 2013.
[13] Thompson, S. J., Farnell, S. C., Farnell, C. C., Farnell, C. C., Andreano, T. M., and Williams, J. D., "Combined Electrostatic Analyzer—Wien Filter Probe for Characterization of Species Distributions in Hall Thrusters," *J Appl Phys*, Vol. 130, No. 23, Dec. 2021, doi: 10.1063/5.0071656.
[14] Hutchinson, I. H., *Principles of Plasma Diagnostics*, 2nd Ed. Cambridge University Press, 2002. doi: 10.1017/CBO9780511613630.
[15] Lemmer, K. M., Gallimore, A. D., Smith, T. B., and Austin, D. R., "Review of Two Retarding Potential Analyzers for Use in High Density Helicon Plasma," *30th International Electric Propulsion Conference*, 2007-161, Florence, Italy, Sep. 2007.
[16] E. Heubel, "Enhancing Retarding Potential Analyzer Energy Measurements with Micro-Aligned Electrodes," Ph.D. Dissertation, Mechanical Engineering, Massachusetts Institute of Technology, Cambridge, MA, 2014.
[17] B. Ferda, "Retarding Potential Analyzer Theory and Design," Princeton Plasma Physics Laboratory, Princeton, NJ, 2015.
[18] C. M. Marrese, N. Majumdar, J. M. Haas, G. Williams, L. B. King, and A. D. Gallimore, "Development of a Single-Orifice Retarding Potential Analyzer for Hall Thruster Plume Characterization," *25th International Electric Propulsion Conference*, 1997-066, Cleveland, OH, Oct. 1997.
[19] R. Sullivan, "The Physics of High-Velocity Ions in the Hall Thruster Near-Field," Ph.D., Aerospace Engineering, California Institute of Technology, Pasadena, CA, 2010.
[20] M. Satir, F. Sik, E. Turkoz, and M. Celik, "Design of the Retarding Potential Analyzer to Be Used with BURFIT-80 Ion Thruster and Validation Using PIC-DSMC Code," *7th International Conference on Recent Advances in Space Technologies (RAST)*, Istanbul, Turkey, 2015.
[21] Chao, C. K. and Su, S. Y., "Charged Particle Motion inside the Retarding Potential Analyzer," *Phys Plasmas*, Vol. 7, No. 1, pp. 101–107, Jan. 2000, doi: 10.1063/1.873817.
[22] Trottenberg, T., Bansemer, F., Hesse, M., Kersten, H., Laube, J., Schneider, V., Schuster, B., Seimetz, L., and Wimmer-Schweingruber, R. F., "The Role of Grid Geometry and Relative Orientation in the Performance of a Retarding Potential Analyzer," *AIP Adv*, Vol. 15, No. 3, Mar. 2025, doi: 10.1063/5.0250806/3339824.
[23] W. Huang, D. M. Ahem, and J. T. Yim, "Lessons Learned from Development of Solar Electric Propulsion Plasma Diagnostics Package," *12th Spacecraft Propulsion JANNAF*, Huntsville, AL, Dec. 2022.
[24] Goebel, D. M., Katz, I., and Mikellides, I. G., *Fundamental of Electric Propulsion*, 2nd Ed. Hoboken, NJ: John Wiley & Sons, 2024.
[25] K. R. Spangenberg, *Vacuum Tubes*. New York City, NY: McGraw-Hill Book Company, 14948.
[26] Williams, J. D., Goebel, D. M., and Wilbur, P. J., "Analytical Model of Electron Backstreaming for Ion Thrusters," *39th AIAA/ASME/SAE/ASEE Joint Propulsion Conference and Exhibit*, AIAA-2003-4560, Huntsville, AL, Jul. 2003. doi: 10.2514/6.2003-4560.
[27] Goebel, D. M. and Becatti, G., "Compact Scanning Retarding Potential Analyzer," *Review of Scientific Instruments*, Vol. 92, No. 1, Jan. 2021, doi: 10.1063/5.0035964.
[28] R. B. Lobbia and A. D. Gallimore, "Fusing Spatially and Temporally Separated Single-Point Turbulent Plasma Flow Measurements into Two-Dimensional Time-Resolved Visualizations," *12th International Conference on Information Fusion Seattle*, Seattle, WA, Jul. 2009.
[29] Durot, C. J. and Gallimore, A. D., "Time-Resolved Laser-Induced Fluorescence Measurements in the Plume of a 6 Kw Hall Thruster with Unperturbed Oscillations," *ICOPS/BEAMS 2014 - 41st IEEE International Conference on Plasma Science and the 20th International Conference on High-Power Particle Beams*, Washington DC: Institute of Electrical and Electronics Engineers Inc., 2015. doi: 10.1109/PLASMA.2014.7012521.
[30] Chaplin, V. H., Lobbia, R. B., Lopez Ortega, A., Mikellides, I. G., Hofer, R. R., Polk, J. E., and Friss, A. J., "Time-Resolved Ion Velocity Measurements in a High-Power Hall Thruster Using Laser-Induced Fluorescence with Transfer Function Averaging," *Appl Phys Lett*, Vol. 116, No. 23, Jun. 2020, doi: 10.1063/5.0007161.

[31] Baird, M., McGee-Sinclair, R., Lemmer, K., and Huang, W., "Time-Resolved Ion Energy Measurements Using a Retarding Potential Analyzer," *Review of Scientific Instruments*, Vol. 92, No. 7, p. 073306, Jul. 2021, doi: 10.1063/5.0039621.
[32] Thomas, A. and Lemmer, K., "Time-Resolved Ion Energy Measurements Using a Retarding Potential Analyzer for Electric Propulsion Applications," *Review of Scientific Instruments*, Vol. 95, No. 2, Feb. 2024, doi: 10.1063/5.0176167/19673885/023505_1_5.0176167.AM.PDF.
[33] Lobbia, R. B. and Gallimore, A. D., "Temporal Limits of a Rapidly Swept Langmuir Probe," *Phys Plasmas*, Vol. 17, No. 7, Jul. 2010, doi: 10.1063/1.3449588/106620.
[34] Lobbia, R. B. and Beal, B. E., "Recommended Practice for Use of Langmuir Probes in Electric Propulsion Testing," *J Propuls Power*, pp. 1–24, 2016, doi: 10.2514/1.B35697.
[35] Sheehan, J. P., Raitses, Y., Hershkowitz, N., and McDonald, M., "Recommended Practice for Use of Emissive Probes in Electric Propulsion Testing," *J Propuls Power*, Vol. 33, No. 3, pp. 614–637, May 2017, doi: 10.2514/1.B35697.
[36] Enloe, C. L. and Shell, J. R., "Optimizing the Energy Resolution of Planar Retarding Potential Analyzers," *Review of Scientific Instruments*, Vol. 63, No. 2, pp. 1788–1791, Feb. 1992, doi: 10.1063/1.1143339.
[37] Nicolle, L., Sarrailh, P., Garrigues, L., Hess, S., and Villemant, M., "Modeling of a Retarding Potential Analyzer and Comparison with Express-A in-Flight Measurements," *Front Phys*, Vol. 10, Oct. 2022, doi: 10.3389/fphy.2022.862945.
[38] Steinier, J., Termonia, Y., and Deltour, J., "Comments on Smoothing and Differentiation of Data by Simplified Least Square Procedure," *Anal Chem*, Vol. 44, No. 11, pp. 1906–1909, Sep. 1972, doi: 10.1021/AC60319A045/ASSET/AC60319A045.FP.PNG_V03.
[39] Savitzky, A. and Golay, M. J. E., "Smoothing and Differentiation of Data by Simplified Least Squares Procedures," *Anal Chem*, Vol. 36, No. 8, pp. 1627–1639, Jul. 1964, doi: 10.1021/AC60214A047/ASSET/AC60214A047.FP.PNG_V03.
[40] W. Huang, G. J. Williams, P. Y. Peterson, H. Kamhawi, J. H. Gilland, and D. A. Herman, "Plasma Plume Characterization of the HERMeS during a 1722-Hr Wear Test Campaign," *35th International Electric Propulsion Conference*, 2017-307, Atlanta, GA, Oct. 2017.
[41] J. T. Yim, W. Huang, and M. G. Allen, "Extraction of Thruster Plume Ion Population Trends from Retarding Potential Analyzer Data," *38th International Electric Propulsion Conference, 2024-116*, 2024-116, Toulouse, France, Jun. 2024.
[42] Hofer, R. R. and Gallimore, A. D., "High-Specific Impulse Hall Thrusters, Part 2: Efficiency Analysis," *J Propuls Power*, Vol. 22, No. 4, pp. 732–740, May 2006, doi: 10.2514/1.15954;PAGE:STRING:ARTICLE/CHAPTER.
[43] Nussbaumer, H. J., *Fast Fourier Transform and Convolution Algorithms*, 2nd Ed. Berlin: Springer, 1982. doi: 10.1007/978-3-642-81897-4.
[44] Petrov, G. M., "A Simple Algorithm for Spectral Line Deconvolution," *J Quant Spectrosc Radiat Transf*, Vol. 72, No. 3, pp. 281–287, Feb. 2002, doi: 10.1016/S0022-4073(01)00125-X.
[45] Hansen, P. C. and O'Leary, D. P., "The Use of the L-Curve in the Regularization of Discrete Ill-Posed Problems," *SIAM Journal on Scientific Computing*, Vol. 14, No. 6, pp. 1487–1503, Nov. 1993, doi: 10.1137/0914086.
[46] Lobbia, R. B., "A Time-Resolved Investigation of the Hall Thruster Breathing Mode," University of Michigan, Ann Arbor, MI, 2010.
[47] Lobbia, R. B. and Gallimore, A. D., "A Method of Measuring Transient Plume Properties," *44th AIAA/ASME/SAE/ASEE Joint Propulsion Conference and Exhibit*, AIAA-2008-4650, Hartford, CT, Jul. 2008. doi: 10.2514/6.2008-4650;JOURNAL:JOURNAL:6.JPC;PAGE:STRING:ARTICLE/CHAPTER.
[48] Durot, C. J., Gallimore, A. D., and Smith, T. B., "Validation and Evaluation of a Novel Time-Resolved Laser-Induced Fluorescence Technique," *Review of Scientific Instruments*, Vol. 85, No. 1, Jan. 2014, doi: 10.1063/1.4856635/356424.
[49] Eckhardt, D., Koo, J., Martin, R., Holmes, M., and Hara, K., "Spatiotemporal Data Fusion and Manifold Reconstruction in Hall Thrusters*," *Plasma Sources Sci Technol*, Vol. 28, No. 4, p. 045005, Apr. 2019, doi: 10.1088/1361-6595/AB0B1F.

[50] Thomas, A., Lemmer, K., and Johnson, L., "Time-Resolved Ion Energy Measurements in the SPT-50 Hall Effect Thruster," *AIAA Science and Technology Forum and Exposition, AIAA SciTech Forum 2025*, AIAA-2025-0909, Orlando, FL: American Institute of Aeronautics and Astronautics Inc, AIAA, Jan. 2025. doi: 10.2514/6.2025-0909.

[51] S. J. Thompson, Z. K. Robertson, S. C. Farnell, C. C. Farnell, C. C. Farnell, and J. D. Williams, "Time-Resolved Ion Measurement in the Beam Plasma of a Hall Thruster," *38th International Electric Propulsion Conference*, 2024-818, Toulouse, France, Jun. 2024.

[52] P. J. Roberts, V. H. Chaplin, and B. A. Jorns, "Time-Resolved Laser Diagnostics in Hall Thrusters with Time-Delay Embedding Data Fusion," *38th International Electric Propulsion Conference*, 2024-596, Toulouse, France, Jun. 2024.

[53] Takens, F., "Detecting Strange Attractors in Turbulence," *Dynamical Systems and Turbulence, Warwick 1980*, D. Rand and L.-S. Young, Eds., Berlin, Heidelberg: Springer Berlin Heidelberg, 1981, pp. 366–381.

[54] Sugihara, G., May, R., Ye, H., Hsieh, C., Deyle, E., Fogarty, M., and Munch, S., "Detecting Causality in Complex Ecosystems," *Science (1979)*, Vol. 338, No. 6106, pp. 496–500, Oct. 2012, doi: 10.1126/science.1227079.

[55] Delavière-Delion, Q., Gaboriau, F., Fubiani, G., and Garrigues, L., "The Effects of Breathing Mode Oscillations on Ion Energy Distribution Function in Hall Thrusters: Time-Resolved RPA Measurements," *Phys Plasmas*, Vol. 31, No. 12, Dec. 2024, doi: 10.1063/5.0235762.

[56] Guglielmi, A., Martin Ortega, A., Gaboriau, F., and Boeuf, J. P., "Influence of Double-Stage Operation on Breathing Oscillations and Rotating Spokes in the ID-HALL Thruster," *36th International Electric Propulsion Conference*, 2019-632, Vienna, Austria, Sep. 2019.

[57] Martín Ortega, A., Guglielmi, A., Gaboriau, F., Boniface, C., and Boeuf, J. P., "Experimental Characterization of ID-Hall, a Double Stage Hall Thruster with an Inductive Ionization Stage," *Phys Plasmas*, Vol. 27, No. 2, Feb. 2020, doi: 10.1063/1.5140241/1062794.

[58] Wei, L., Li, W., Ding, Y., Han, L., Yu, D., and Cao, Y., "Study on Ion Energy Distribution in Low-Frequency Oscillation Time Scale of Hall Thrusters," *The European Physical Journal Plus*, Vol. 132, No. 11, p. 452, Nov. 2017, doi: 10.1140/epjp/i2017-11714-3.

[59] Choueiri, E. Y., "Plasma Oscillations in Hall Thrusters," *Phys Plasmas*, Vol. 8, No. 2001, pp. 1411–1426, 2001, doi: 10.1063/1.1354644.

[60] Ochoukov, R., Dreval, M., Bobkov, V., Faugel, H., Herrmann, A., Kammerloher, L., and Leitenstern, P., "'Ion Temperature Measurement Techniques Using Fast Sweeping Retarding Field Analyzer (RFA) in Strongly Intermittent ASDEX Upgrade Tokamak Plasmas,'" *Review of Scientific Instruments*, Vol. 91, No. 7, Jul. 2020, doi: 10.1063/5.0019839.

[61] Shastry, R., Hofer, R. R., Reid, B. M., and Gallimore, A. D., "Method for Analyzing E×B Probe Spectra from Hall Thruster Plumes," *Review of Scientific Instruments*, Vol. 80, No. 6, Jun. 2009, doi: 10.1063/1.3152218.

[62] Huang, W., Kamhawi, H., Haag, T., Lopez Ortega, A., and Mikellides, I. G., "Facility Effect Characterization Test of NASA's HERMeS Hall Thruster," *52nd AIAA/SAE/ASEE Joint Propulsion Conference*, 2016-4828, Salt Lake City, UT: American Institute of Aeronautics and Astronautics, Jul. 2016. doi: 10.2514/6.2016-4828.

[63] Dunn, P. F. and Davis, M. P., *Measurement and Data Analysis for Engineering and Science*, 4th Ed. New York City, NY: CRC Press, 2017. doi: 10.1201/b22182.

[64] Van De Ven, T. H. M., De Meijere, C. A., Van Der Horst, R. M., Van Kampen, M., Banine, V. Y., and Beckers, J., "Analysis of Retarding Field Energy Analyzer Transmission by Simulation of Ion Trajectories," *Review of Scientific Instruments*, Vol. 89, No. 4, Apr. 2018, doi: 10.1063/1.5018269/362131.